R-06-108

Effect of the mineral precipitation-dissolution at tunnel walls during the operational and post-operational phases

Cristina Domènech, David Arcos,
Lara Duro, Fidel Grandia
Enviros, Spain

November 2006

Svensk Kärnbränslehantering AB
Swedish Nuclear Fuel
and Waste Management Co
Box 5864
SE-102 40 Stockholm Sweden
Tel 08-459 84 00
+46 8 459 84 00
Fax 08-661 57 19
+46 8 661 57 19

ISSN 1402-3091
SKB Rapport R-06-108

Effect of the mineral precipitation-dissolution at tunnel walls during the operational and post-operational phases

Cristina Domènech, David Arcos,
Lara Duro, Fidel Grandia
Enviros, Spain

November 2006

Abstract

The extent of reversibility of the geochemical conditions disturbed during the construction and operational phases is of importance in order to assess the chemical evolution of the repository system. In this regard, it is essential to have a deep understanding of the chemical status of the repository system at closure in order to describe its immediate geochemical evolution beyond this point.

This project assesses the dissolution and precipitation of minerals due to the interaction with groundwater in the deposition tunnel wall-rock during the operational phase (prior to tunnel backfilling) and during the saturation phase, also considering the effect on the backfill material.

We have performed a 2D model in which a fracture intersecting the main tunnel has been considered. The project has been developed in two consecutive stages. The first stage simulates the precipitation and dissolution of minerals in the tunnel wall rock during the operational phase (100 years after excavation) when the tunnel is empty and filled with air. During this stage, water flows through fractures into the tunnel. The results of the model suggest that the interaction between groundwater, fracture-filling minerals, and atmospheric $O_2(g)$ and $CO_2(g)$ present in the tunnel leads to the precipitation of secondary minerals (calcite and iron(III) oxy-hydroxide) that do not significantly affect the porosity of the area surrounding the tunnel.

The second stage starts after the operational phase, once the tunnel is backfilled, and simulates the interaction of groundwater with fracture-filling minerals and the backfill material. The model implemented assumes that the backfill is already water saturated and that water flows following the regional head gradient. Moreover, it also assumes that $O_2(g)$ is still present in the tunnel wall, as a result of the operational phase disturbances. The results show that oxygen will oxidise pyrite in the backfill and promote the precipitation of $Fe(OH)_3(am)$ during the first 200 years and that the redox control is exerted by the pair $Fe(II)/Fe(OH)_3(am)$. The extent of pyrite oxidation, pH value and the length of the transitory state prior to achieving a new steady state in the system are clearly influenced by the presence of carbonate minerals (calcite and siderite) and microbially mediated organic matter oxidation. Different sensitivity analyses have been performed to detail these effects.

Contents

1 Introduction

The extent of reversibility of the geochemical conditions disturbed during the construction and operational phases is of importance in order to assess the chemical evolution of the repository system. This is recognised in the planning report of the SR-Can performance assessment of long-term safety for a KBS-3 repository /SKB 2003/. In this regard, as it is acknowledged in the aforementioned report, it is essential to have a deep understanding of the chemical status of the repository system at closure in order to describe its immediate geochemical evolution beyond this point.

One of the issues of concern is the effect of precipitation and dissolution of minerals during the operational phase due to the inflow of groundwater into the deposition tunnel and to mixing of different water types. However, there are no clear indications about the extent of the perturbations and the recovery time.

The present study has been performed to assess the effect of dissolution and precipitation of primary and secondary accessory minerals on the geochemical evolution of the deposition tunnels and surrounding rocks prior and after they have been backfilled (operational and post-operational stages).

In this report the conceptual model on the geochemical evolution of deposition tunnels and modelling results are presented. We also present the results of a sensitivity analysis performed to assess the importance of some of the main uncertainties of the conceptual model.

2 Objectives and methodology

The main objective of this project is to study the precipitation and dissolution of minerals due to the interaction with groundwater in the deposition tunnel wall-rock during the operational phase (prior to tunnel backfilling) and during the saturation phase, also considering the effect on the backfill material.

The project has been developed in two consecutive stages, which are detailed below:

First stage: The first stage simulates the precipitation and dissolution of minerals on the tunnel wall rock during the operational phase, that is, for a period of approximately 100 years after excavation, when the tunnel is empty and open to air (Figure 2-1a). During this stage, water flows through fractures into the tunnel. The interaction between groundwater, fracture-filling minerals, and atmospheric pressures of $O_2(g)$ and $CO_2(g)$ present in the tunnel may lead to precipitation and/or dissolution of different minerals in the tunnel wall rock. These precipitation/dissolution processes may affect the hydrogeological properties of the area surrounding the tunnel.

Second stage: The second stage starts after the operational phase, once the tunnel is backfilled. Due to code limitations, the model implemented will assume that the backfill is already water saturated, i.e., the saturation stage is not simulated. In this case, water flows following the regional head gradient (Figure 2-1b). After the backfilling of the tunnel, the geochemical conditions, especially the redox conditions of the tunnel wall, will have changed from the oxidized state achieved after stage 1 to a more reducing state. In case of the formation of an excavation disturbed zone (EDZ) during the tunnel construction, the presence of high concentrations of $O_2(g)$ in the water at the rock wall is expected, giving its higher hydraulic conductivity. Thus, in this second stage we will consider that the rock in contact with the tunnel is still oxidized and that its water still contains $O_2(g)$. As initial conditions we will use the final state achieved in the first stage of the model, giving that they will be consistent with these $O_2(g)$ conditions. The reason of following this approach is to simplify the intermediate stage between the emplacement of the backfill and its saturation.

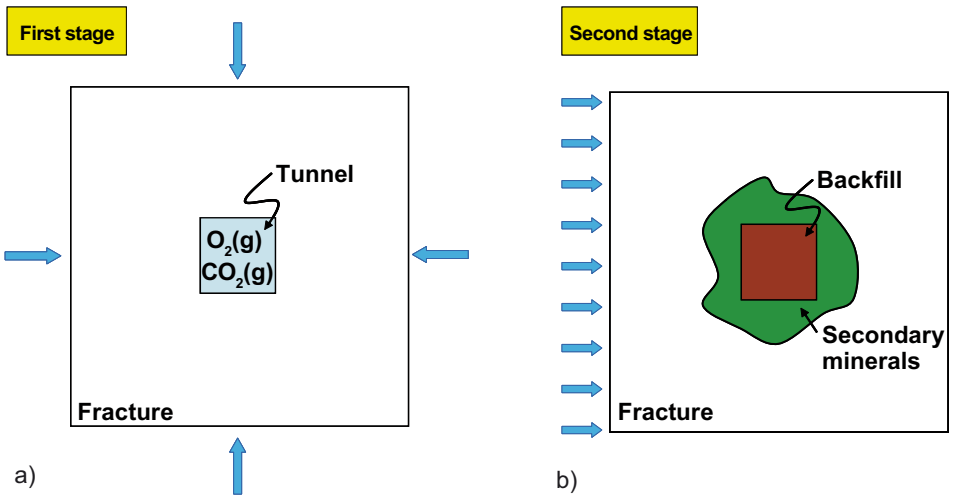

Figure 2-1. *Schematic design of the two sequential stages of the model.*

3 The geochemical system

The presence of the repository would induce some significant changes, especially in the groundwater and mineral composition around the tunnel.

During the operational period of the repository, changes in the groundwater composition due to the presence of the tunnel open space, may give rise to the precipitation of new minerals and/or dissolution of the ones already existing in the fracture-fillings and in the tunnel walls. These changes may affect both the geochemistry and/or the hydrology of the backfill once the tunnel is filled. Thus, it is essential to understand the chemical status of the repository system at closure in order to describe its immediate geochemical evolution /SKB 2004a/.

Fractures represent the main flowing pathways for groundwater in this type of fractured media. /Petersson et al. 2004/ provide a detailed study of the first four drill cores obtained in the Forsmark site, including the characterisation and identification of a number of fracture-filling minerals. Their study shows that quartz and albite (± K-feldspars) as well as chlorite and calcite are present in most of the samples. Additional minerals identified are: prehnite, which occurs in some fracture-fillings together with analcime and laumontite, pyrite, frequently found, and hematite, which is common but in relatively low amounts. The presence of epidote, apophyllite, and fluorite, as well as some mixed-layer clays, such as corrensite, illite and saponite is also reported.

/Luukkonen et al. 2004/ conducted an estimation on which is the effect of the underground excavations in the Olkiluoto bedrock on naturally occurring fracture mineral buffers. The authors consider different groundwater types (meteoric water, seawater and a mixture of both) as recharging waters in their equilibrium geochemical calculations. /Luukkonen et al. 2004/ used the PHREEQC code to conduct their 1D calculations, very similar to the ones presented in 1999 by /Guimerà et al. 1999/. /Luukkonen et al. 2004/ assumed the dissolution of pyrite controlled by kinetics, as it is expected to occur due to the generally slow kinetics of this process under near-neutral pH conditions.

They tested different models by using meteoric water as recharging water type, containing inorganic carbon due to the oxidation of organic matter in the soil. In the absence of calcite in the system, pyrite dissolved producing an important pH decrease (from 5.4 to 3.9), while pyrrhotite dissolution produced only minor changes in pH. Both processes consumed oxygen thus causing the evolution of the system towards reducing conditions. In the case of assuming that calcite was present, the decrease of pH was buffered, what produces the precipitation of Fe(III) released from the dissolution of iron sulphides.

When assuming that rainwater flowed directly through the fractures, without having experimented any modification of its composition due to organic matter oxidation in the soil layers, the dissolution of pyrite by oxygen consumption caused calcite dissolution although, due to the lower DIC content of rainwater, the extent of calcite dissolution was lower than in the previous cases. An important effect of this simulation was the higher pH value achieved (up to 9).

When assuming that the recharging water had flown through soils with a very high organic respiration, thus containing higher carbonate and lower oxygen concentrations, the results indicated the highest calcite dissolution. This is due to the fact that, besides the dissolution of calcite driven by acidification through sulphide oxidation, the high pCO_2 contributed to calcite dissolution.

The overall conclusion from the equilibrium calculations conducted by these authors is that the highest risk for depletion of buffering minerals in the system was meteoric recharge, what can be in concordance with the low mineralized water infiltration expected from glacial melt-water. Furthermore, they highlighted that biogenic CO_2 would pose a stronger risk on the calcite buffer

than those processes related to dissolved O_2 of recharging meteoric water. This is not surprising, since the effect that oxygen can have on the depletion of calcite in the system is only indirect, through the oxidation of pyrite that will cause acidification and it will be this acidification what would cause calcite dissolution. Nevertheless, a high pCO_2 in the system would increase calcite solubility and thus induce a faster calcite depletion in the system.

On the basis of the equilibrium calculations, the authors estimated the half-life for the buffering minerals in the fractures. They followed a methodology based on the estimated coating thickness of calcite and pyrite on the fractures in combination with the equilibrium calculations presented above. The conclusion from their calculations was that slow flow rates of groundwater did not create significant losses of buffering minerals. Nevertheless, as discussed in their report, i) the simulations were extremely simple, in the sense that they did not consider other processes acting in the system that could account for oxygen consumption and/or pH buffering and ii) the assumptions taken were rather unrealistic, given that they considered that the water reaching the fracture infillings had not been modified due to other geochemical processes acting at shallower depths.

The results of the simulations presented in /Luukkonen et al. 2004/ are similar to the ones shown in /Guimerà et al. 1999/. /Guimerà et al. 1999/ assumed the infiltration of a very low mineralized groundwater (exemplifying glacial melt-water) through a fracture by using the PHREEQC code. In those calculations, the influence of different minerals on the buffering of an oxic intrusion was assessed by following two different approaches: i) the stationary state-approach and ii) the equilibrium approach by using the PHREEQC code. Different minerals were assumed to have an effect on the oxygen intrusion: pyrite and Fe-bearing chlorite. The results indicated that in the case of having chlorite in the fractures, the time for the complete depletion of chlorite down to repository depths was over 100,000 years in the worst case of assuming a fast and direct fracture connecting the surface with the repository. Calcite was always able to buffer pH and it was never depleted in the system in the case of assuming that the oxic intrusion was being buffered by chlorite.

On the other hand, when assuming that pyrite was the main mineral accounting for oxygen consumption, as in the /Luukkonen et al. 2004/ case, /Guimerà et al. 1999/ reported that the oxic intrusion would not reach the repository depths until 10 million years after the initiation of the infiltration.

In that work, /Guimerà et al. 1999/ highlighted some of the drawbacks associated to the equilibrium assumption in PHREEQC (discretisation of the system number of cells, dispersion term, residence time of water), and justified the use of a more complex modelling for the assessment of the rate of intrusion of the redox front and its associated buffering-minerals depletion in the media. Thus, an analyses of the reaction times versus flow rates allowed to conclude that a kinetic approach would be more realistic when dealing with the type of slow processes normally associated with electron transfer reactions, such as pyrite and/or Fe-bearing silicates oxidation. Finally, a 2D modelling was therefore implemented into a reactive transport code that was later refined in /Guimerà et al. 2006/.

The methodology followed in /Luukkonen et al. 2004/, thus, results in a very good way of assessing general trends of the system regarding to buffering minerals but lack of a more detailed description of some processes that may be of importance. The complexity of the geochemical system should be increased, by incorporating other oxygen consumption processes and pH buffering effects.

According to this, the interaction of groundwater flowing through fractures with $O_2(g)$ and $CO_2(g)$ present in the tunnel during the operational period will cause changes in the water composition and in the mineralogy of the system near the tunnel wall. Oxidation of Fe(II) will probably cause precipitation of $Fe(OH)_3(am)$ and the decrease of pCO_2 of groundwater to atmospheric values, the precipitation of calcite.

From a qualitative perspective, we can predict that once the tunnel has been backfilled the introduction or removal of aqueous Ca from the pore water will affect the cation exchange process of the system, given the percentage of bentonite present in the backfill. The cation exchange capacity of host rock minerals is low when compared to those of the backfill minerals, and therefore this process is only relevant for the clay fraction of the backfill /Pusch 2001/.

Carbonate precipitation, together with sulphates and silica compounds, can also contribute to cementing the medium.

During the operational and post-operational periods some microbes can take advantage of the changing conditions and consume part of the organic materials or stray organic compounds left in the repository during the operational phase. An overview of these processes and their consequences is needed when discussing other non-microbial processes occurring during operation and the time immediately after closure /SKB 2004a/.

4 STAGE 1. Modelling of the operational phase

4.1 Conceptual model

4.1.1 Modelled domain and hydrodynamic system

No final decision on the technique for the excavation of the deposition tunnel has been taken so far /SKB 2004b/. Thus, SR-Can analyses two alternative techniques:

i) Drilling and blasting. This will lead to a square deposition tunnel with an arched roof (5.5 m×5.5 m),

ii) Mechanical excavation (TBM). In this case, the deposition tunnel will have a circular cross section (from 6 to 6.5 m in diameter).

In order to simplify the implementation of the model, the vertical section of the tunnel is considered as a square of 6 m side-length. Thus, the modelled domain consists on a 2D squared field of 40 m centred at and perpendicular to the tunnel section. The effect of deposition holes is neglected, as they represent only 0.1% of the total volume /SKB 2004b/.

In the operational stage the tunnel is empty and water flows into the tunnel from conductive fractures in the host rock. For this reason the 2D model considers a fracture plane in the rock which is intersected perpendicularly by the tunnel. Thus, water flows into the tunnel from the fracture due to hydraulic head gradients (Figure 4-1).

The model will be run for 100 years, the expected length of the operational phase.

4.1.2 Mineralogical and chemical system

Water flowing through the fractures is considered equal to deep groundwater analysed at Forsmark (Table 4-1). No quantitative mineralogical analyses of the fracture-fillings are available so far. The fracture-filling minerals that can play a role in the geochemical characteristics of the tunnel wall are pyrite and calcite. As the report of /Petersson et al. 2004/ does not include any quantification of the mineral composition of Forsmark fracture-fillings, we have used data in /Dershowitz et al. 2003/ on Äspö fractures to estimate the amount of calcite and pyrite in the fractures. The results are listed in Table 4-2.

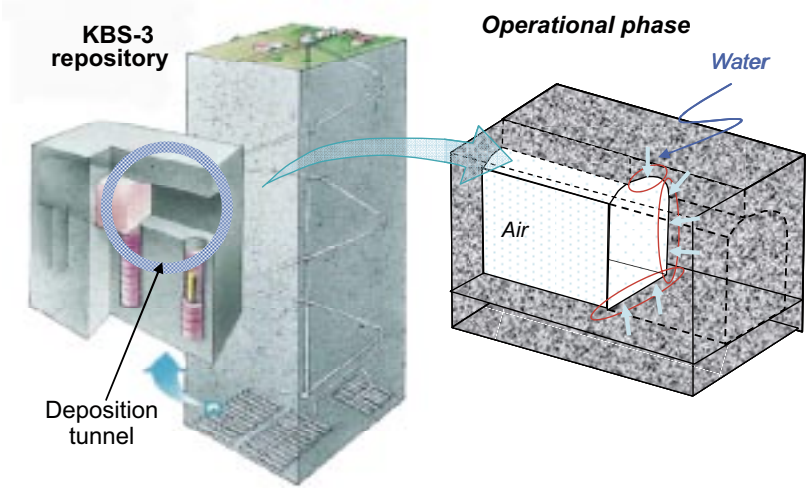

Figure 4-1. *Drawing of the KBS-3 concept of deep disposal of high level nuclear waste (HLNW). During the operational phase, water flowing to the tunnel can modify the mineralogical and chemistry system of the tunnel wall.*

Table 4-1. Forsmark groundwater composition. All concentrations, except pH are total concentrations in mole dm^{-3} water; $fO_2(g)$ in atm. Data from borehole KFM02A, at 512 m depth /from SKB 2004a/.

Components	Forsmark
pH	7.2
Na	0.089
Ca	0.023
Mg	0.0093
K	0.0009
Fe(II)	$33 \cdot 10^{-6}$
HCO_3^-	0.0022
Cl^-	0.153
SO_4^{2-}	0.0052
HS^-	≈ 0
$fO_2(g)$	<< 10^{-20}
Ionic strength	0.19

Table 4-2. Fracture mineral composition, in %wt. /from Dershowitz et al. 2003, Petersson et al. 2004/.

Mineral	% wt
Calcite	11.5
Pyrite	0.04

The temperature of the system is considered constant and equal to 15°C, thus gypsum instead of anhydrite is preferred to represent calcium sulphate as secondary mineral able to precipitate in case that it becomes oversaturated. Other secondary minerals allowed to form during the simulation are siderite, amorphous iron sulphide (FeS) and amorphous $Fe(OH)_3$. No silicate bearing minerals have been considered, given that their dissolution rate is too slow when compared to the short time-length of the simulation (100 years).

Processes such as aqueous complexation in solution and dissolution and/or precipitation of secondary minerals are considered fast reactions that rapidly achieve equilibrium (equilibrium constants listed in Table 4-3).

Pyrite oxidation (Equation 1) is considered a kinetically controlled process that follows Equation 2 /Williamson and Rimstidt 1994/. Under the chemical conditions expected at the fracture-tunnel boundary, pyrite is far from equilibrium (SI = –243), thus we do not consider the effect of the saturation degree of pyrite on the dissolution kinetics. No temperature changes are modelled in the system and, therefore, no activation energy term is included in the dissolution rate law.

$$FeS_2\,(s) + 3.75\,O_2\,(aq) + 3.5\,H_2O \rightarrow Fe(OH)_3\,(am) + 2\,SO_4^{2-} + 4H^+ \qquad \text{Equation 1}$$

$$r\left(\frac{mol}{m^2 s}\right) = 10^{-8.19(\pm 0.10)} \frac{\left[O_2(aq)\right]^{0.50(\pm 0.04)}}{\left[H^+\right]^{0.11(\pm 0.01)}} \qquad \text{Equation 2}$$

Table 4-3. Mineral processes considered in the model, including dissolution reactions, logK(25°C) and ΔH_r. If ΔH_r is not specified, no value was found in the literature and a value of 0.0 kJ·mol^{-1} is used. Data come from /Hummel et al. 2002/, except other source reported.

Primary minerals Mineral	Reaction
Pyrite	**$FeS_2 + H_2O = 0.25\ H^+ + 0.25\ SO_4^{2-} + Fe^{2+} + 1.75\ HS^-$** log K_{eq} = –26.91 ΔH_r = 308.8 kJ mol^{-1}
Calcite	**$CaCO_3 = CO_3^{2-} + Ca^{2+}$** log K_{eq} = –8.480 ΔH_r = –9.6 kJ mol^{-1}
Secondary minerals **Mineral**	**Reaction**
Siderite	**$FeCO_3 = Fe^{2+} + CO_3^2$** log K_{eq} = –10.8 ΔH_r = –22.3 kJ mol^{-1}
Gypsum	**$CaSO_4{:}2H_2O = Ca^{2+} + SO_4^{2-} + 2\ H_2O$** log K_{eq} = –4.58 ΔH_r = 1.5 kJ mol^{-1}
$Fe(OH)_3$(am)	**$Fe(OH)_3 + 3\ H^+ = Fe^{3+} + 3\ H_2O$** log K_{eq} = 4.9 ΔH_r = –84.1 kJ mol^{-1}
FeS(ppt)	**$FeS + H^+ = Fe^{2+} + HS^-$** /Falck et al. 1996/ log K_{eq} = –3.915

Water flowing into the tunnel will face a constant atmospheric pressure of O_2(g) and CO_2(g) during the operational phase. This will cause an increase of the O_2(aq) in the tunnel wall that will enhance the oxidation of some minerals, such as that of pyrite. The formation of pyrite occurs through a mechanism of sulphidation of amorphous and crystalline compounds with the general formula FeS that are formed directly from solution /Rickard 1975/. Therefore and given the short simulation times studied here, we have assumed that FeS(am) forms predominantly instead of pyrite in case of oversaturation.

CO_2(g) partial pressure will control the precipitation of calcite in the tunnel wall according to Equation 3 together with Ca concentration, which will be also affected by the precipitation of gypsum, if oversaturated (Equation 4).

$$Ca^{2+} + CO_2(g) + H_2O \leftrightarrow CaCO_3(s) + 2\ H^+ \qquad \text{Equation 3}$$

$$Ca^{2+} + SO_4^{2-} + 2\ H_2O \leftrightarrow CaSO_4 \bullet 2H_2O\ (s) \qquad \text{Equation 4}$$

Iron produced by pyrite oxidation, as well as the initial iron content of the Forsmark groundwater can precipitate as siderite (Equation 5) or amorphous $Fe(OH)_3$ (Equation 6) depending on the redox potential and the pH of the system.

$$Fe^{2+} + HCO_3^- \rightarrow FeCO_3\ (s) + H^+ \qquad \text{Equation 5}$$

$$4\ Fe^{2+} + O_2(aq) + 10\ H_2O \rightarrow 4\ Fe(OH)_3\ (am) + 8\ H^+ \qquad \text{Equation 6}$$

No microbial influence has been included in the reference system.

4.2 Numerical model

4.2.1 Code capabilities

The numerical problem has been solved by using the code PHAST /Parkhurst et al. 2004/ which is the result of coupling a transport code, HST3D /Kipp 1997/ and a geochemical code, PHREEQC /Parkhurst and Appelo 1999/. The reaction-transport equations are solved by sequential approach in which solute transport and chemical reaction are divided into separate calculations for each time step. First, the components are transported and then geochemical reactions are calculated. PHAST uses porous media properties and boundary conditions defined by zones for a point-distributed-finite-difference grid.

4.2.2 Grid and time discretization

The two-dimensional model has 17,298 nodes, defining a volume of 40 m×40 m×0.4 m centred in the tunnel section, which has been considered a square of 6 m side length. The grid is heterogeneous with grid spacing varying from 2 m to 0.1 m, with a higher discretisation in and around the tunnel (Figure 4-2). Thus the cells inside the tunnel are 0.1×0.1 m, and the first fracture cell in contact with the tunnel has a width of 0.25 m.

The estimated duration of the operational phase is 100 years. To avoid numerical problems the time steps increase gradually from 0.01 years to 4 years as the simulation proceeds.

4.2.3 Hydrodynamic properties

Conductivity values for deep fractures are still uncertain. /Hartley et al. 2004/ used both discrete fracture network (DFN) and continuous porous media (CPM) models on a range of scales to investigate the groundwater flow and radionuclide transport from a deep disposal facility to the biosphere. Transmissivity values reported for the fracture network considered in their model range from $9\cdot10^{-9}$ to $6\cdot10^{-7}$ m^2s^{-1}. The same authors calculated the equivalent intrinsic permeabilities (k_i) for the CPM models resulting in values from 10^{-19} to 10^{-14} m^2. However, most of fractures placed between 300 and 500 m depth lie in the range 10^{-16}–$10^{-14.5}$ m^2. According to Equation 7, where K is the hydraulic conductivity, g the gravity (9.81 m s^{-2}), μ the water viscosity ($2.1\cdot10^{-6}$ kg m^{-1} s^{-1}) and ρ_l the water density (1,000 kg m^{-3}), the reported values results in hydraulic conductivities of $5\cdot10^{-7}$ m s^{-1} to $1\cdot10^{-5}$ m s^{-1}.

$$K = \frac{g\rho_l}{\mu} k_i \qquad \text{Equation 7}$$

In the simulation, a value of $5\cdot10^{-7}$ m s^{-1} has been considered for the fracture zone.

In agreement with the study of /Dershowitz et al. 2003/, Äspö fractures have been assumed to have a porosity of 20%.

We have assumed a set of fictitious cells in the inner part of the tunnel that act as reservoirs for a pool of atmospheric O_2(g) and CO_2(g). We assigned to this zone a hydraulic conductivity of 100 m s^{-1} and a porosity of 0.99 in order to simulate an open space.

Effective diffusion coefficient for all solutes has been assumed to be 10^{-10} m^2 s^{-1} /Ochs and Talerico 2004/.

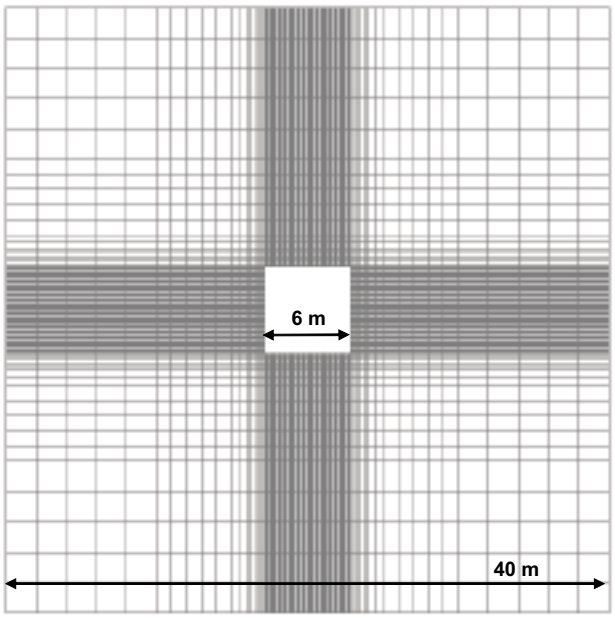

Figure 4-2. *Grid used in the first modelling stage.*

4.2.4 Chemical properties

Groundwater entering the system is the groundwater equilibrated with the fracture-filling minerals; in this case, calcite and pyrite. Thus, initial and boundary groundwater have the same composition (Table 4-4).

When comparing the composition of this groundwater with that of the Forsmark reference water (Table 4-1), the only noticeable difference is in pH, which decreases from 7.2 to 7.08, as a result of the slight oversaturation of the reference water with respect to calcite.

The initial amounts of calcite and pyrite considered in the system are listed in Table 4-2. No information is available about the pyrite reactive area. Some values for pyrite reactive area can be found in literature but they span over some orders of magnitude, depending on the origin of pyrite and the methodology used to obtain this parameter. Pyrite identified in fracture filling materials by /Petersson et al. 2004/ is present as single tiny and idiomorphic crystals in the range of 0.1–0.3 mm side length. The corresponding geometrical area is thus between 0.004 and 0.012 $m^2\ g^{-1}$, although the real reactive area can be 3 or 4 times higher given the irregularities and crystal defects.

Several secondary minerals are allowed to precipitate in the system if they become oversaturated: gypsum, siderite, FeS and $Fe(OH)_3(am)$.

As said previously in Section 4.1.2, temperature is constant and equal 15°C.

4.2.5 Boundary conditions

The model for the first stage of the simulation assumes that groundwater flows from the fracture into the tunnel. The groundwater inflow to the open tunnel has been estimated by using the fracture density. According to /Borgesson et al. 2004/ the fracture density varies from 10^{-3} to 0.02 cm per cm of tunnel. In our model we have assumed a fracture density of 0.01 cm per cm of tunnel, which is equivalent to one fracture of 1 cm aperture perpendicularly intersecting the tunnel every metre of tunnel length.

A prescribed hydraulic head of 500 m has been imposed at the four external boundaries; whereas, at the tunnel wall a head of 0 m has been fixed forcing water to flow towards the tunnel. This implies that the gradient will not be constant in all the domain, given that it increases near the tunnel. An equivalent linear gradient will be 29 m m^{-1}. The input flow under these conditions is $1.1 \cdot 10^7$ kg water/yr. Taking into account the thickness of the modelled volume (0.40 m) and the assumed density of fractures in the tunnel, this input flow to the tunnel is equivalent to 0.52 $dm^3\ min^{-1}$ (m of tunnel length)$^{-1}$. This value agrees with the saturation volume calculated by /SKB 2004b/ if the hydraulic conductivity of the fracture is assumed equal to $5 \cdot 10^{-7}$ m s^{-1}.

Table 4-4. Forsmark groundwater composition in equilibrium with calcite and pyrite. All concentrations, except pH and redox potential, are total concentrations in mole dm^{-3} water.

Components	Mole dm^{-3}
pH	7.08
pe	–2.59
Eh (mV)	–149.5
Na	$8.90 \cdot 10^{-2}$
Ca	$2.30 \cdot 10^{-2}$
Mg	$9.30 \cdot 10^{-3}$
K	$9.00 \cdot 10^{-4}$
Fe(II)	$3.30 \cdot 10^{-5}$
HCO_3^-	$2.15 \cdot 10^{-3}$
Cl^-	$1.53 \cdot 10^{-1}$
SO_4^{2-}	$5.20 \cdot 10^{-3}$
Si	$1.85 \cdot 10^{-4}$

A fixed groundwater composition is imposed at the external boundary while the solution composition is allowed to change as a consequence of the chemical reactions considered at the tunnel boundary.

4.2.6 Initial conditions

The boundary groundwater composition and the groundwater and mineral composition of the system at the initial conditions have been described previously in Section 4.2.4.

4.2.7 Results

As a result of the forced hydraulic gradient, water flows from the border of the system into the tunnel according to the velocity field shown in Figure 4-3. The achieved velocities are about 1,400 m yr^{-1} in the mid external boundary and about 4,000 m yr^{-1} next to the tunnel.

Water entering the tunnel from the fracture plane is initially reductive and in equilibrium with pyrite and calcite. After contacting the concentration of $O_2(aq)$ in equilibrium with the atmospheric $O_2(g)$ partial pressure (conditions at the tunnel boundary), aqueous Fe(II) is oxidised to Fe(III), and this precipitates as $Fe(OH)_3(am)$ (Equation 6). In Figure 4-4a, we have plotted the evolution of the pH and of the redox potential of groundwater when reaching the tunnel wall. The evolution of the redox potential and pH as a function of the distance to the tunnel is plotted in Figure 4-5. As it can be seen the pH and redox conditions of groundwater at the tunnel wall fall in the stability field of $Fe(OH)_3(am)$ due to the increase of redox potential by the $O_2(g)$ content.

Diffusion of dissolved oxygen from the tunnel boundary to the fracture is counteracted by the process of advection of water from the fracture to the tunnel. Therefore, pyrite present in the fracture is not oxidised. Only in the case of considering lower hydraulic conductivies ($< 10^{-10}$ m s^{-1}), diffusion processes will have some influence near the tunnel wall.

There is no back diffusion of $CO_2(g)$ from the tunnel to the fracture plane, either. Water coming from the fracture and in equilibrium with calcite (at $pCO_2(g) = -2.2$) finds a lower $pCO_2(g)$ of –3.5, causing the precipitation of calcite. According to Figure 4-4b, equilibrium with calcite at a pCO_2 of –3.5 increases the pH to values close to 8 as observed in Figure 4-5.

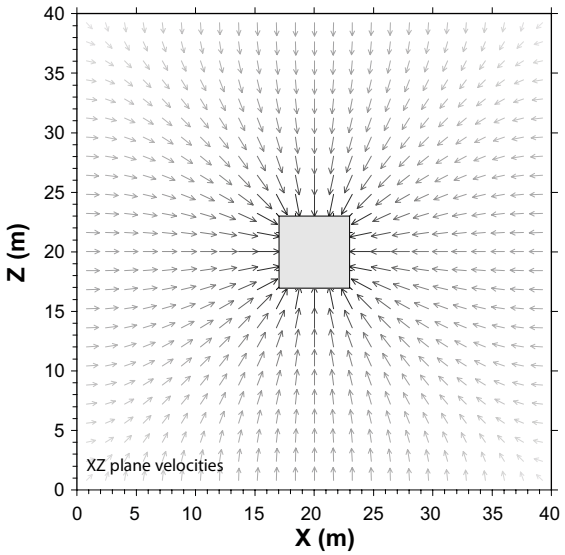

Figure 4-3. *Velocity field obtained by using the boundary conditions specified in Section 4.2.5. Arrow sizes are proportional to the velocity magnitude.*

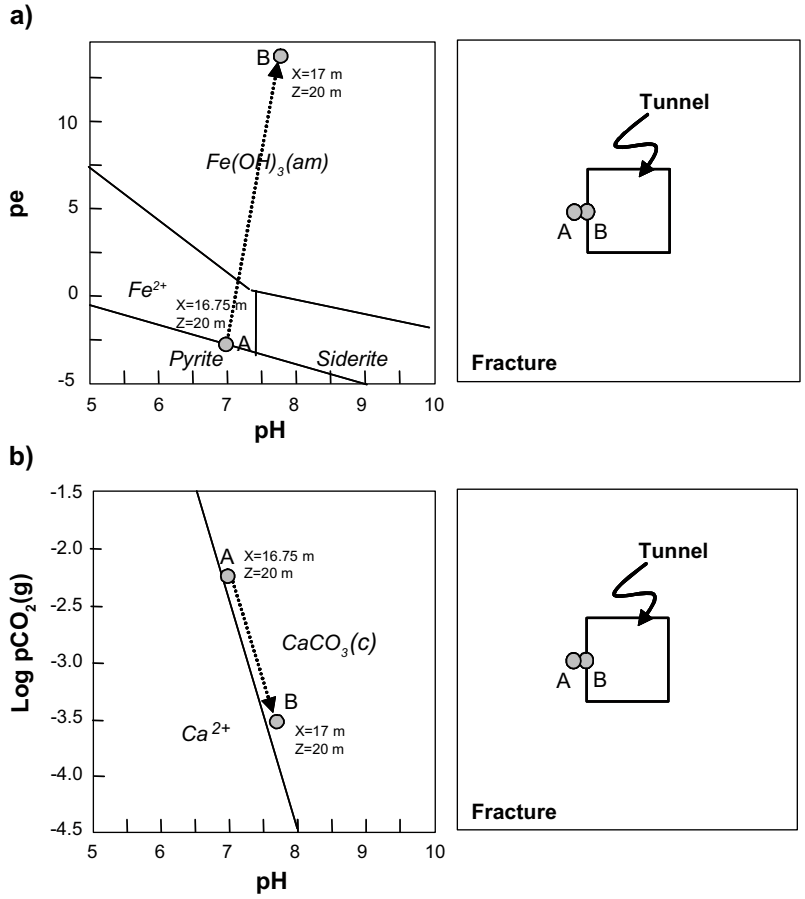

Figure 4-4. *a) Predominance (pe-pH) diagram of the Fe system, showing the evolution of these parameters in groundwater at the contact with the tunnel wall ($[Fe(II)]_{tot} = 3.3 \cdot 10^{-5}$M). Time = 100 years. The redox potential is expressed as pe = Eh(mV)/0.2T. b) Predominance diagram (Log pCO_2(g) vs pH) showing the evolution of these parameters along the calcite boundary at the contact with the tunnel wall ([Ca]tot = $2.23 \cdot 10^{-2}$M). Time = 100 years. Points A and B correspond to the groundwater compositions prior to and just after reaching the tunnel wall, respectively.*

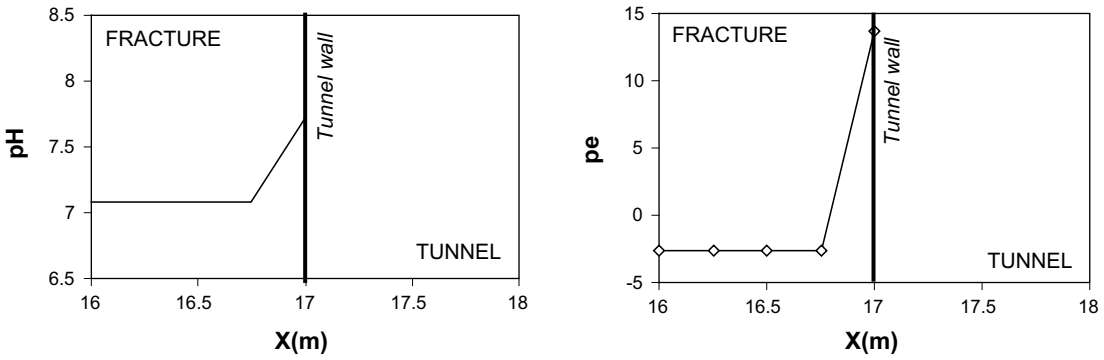

Figure 4-5. *Evolution of pH and redox potential in terms of pe (pe = Eh(mV)/0.2T) at the tunnel wall and at the end of the run (time = 100 y) (Z = 20 m).*

Thus, $Fe(OH)_3(am)$ and $CaCO_3$ precipitate at the contact with the tunnel wall. In Figure 4-6 the amount of precipitated minerals is plotted versus time. The total concentration of iron hydroxide precipitated after the 100 years of simulation is $5.3 \cdot 10^{-3}$ mole·dm^{-3} water and the total amount of calcite is of 0.11 mole·dm^{-3} water. Given the grid and the discretisation of the model, the precipitation of these minerals occurs in a zone comprising the fracture wall, that have a total volume of 1.68 m^3 (the concentrations are given for the grid nodes, and the volume represented in each node in this case includes half of the 0.1 m thick tunnel cell, and half of the 0.25 m thick fracture cell; the total volume for the tunnel intersection is therefore $4 \cdot (6\ m \cdot (½(0.25+0.1)\ m) \cdot 0.4\ m)$. According to the porosities used in the system this volume contains 0.72 m^3 of water and the total amount of minerals precipitated are 71.5 moles of calcite and 3.5 moles of $Fe(OH)_3(am)$.

The distribution of the precipitated minerals around the tunnel is homogeneous.

By taking into account the molar volume of these minerals (36.93 cm^3/g and 34.36 cm^3/g for calcite and $Fe(OH)_3(am)$ respectively) and assuming the formation of a homogeneous layer newly precipitated minerals onto the surface of the tunnel wall, we can calculate an average thickness of calcite on the tunnel of 0.2 mm and an average thickness of 10 μm of $Fe(OH)_3(am)$.

These values are in agreement with values of surface coatings on fractures determined in deep fractures in crystalline media, as indicated in /Luukkonen et al. 2004/.

From experimental observations at the Äspö tunnel, it seems that calcite is not formed on the tunnel walls, but possibly in the fracture. In this modelled case, the groundwater in the fracture is equilibrated with calcite, and, there are no changes of the water composition flowing through the fracture, due to the high advective velocities, therefore, the changes are observed at the tunnel wall, and not inside the fracture. This is probably an artefact of the modelling approach but would indicate the possibility of precipitation of calcite in the surroundings of the tunnel walls. According to the numerical results obtained, the precipitation of these minerals during the operational stage of the repository does not seem to alter significantly the porosity of the tunnel walls and, therefore, no hydraulic conductivity changes are predicted. This effect on the porosity may be even lower if we consider that the actual initial porosity in the fracture will be higher close to the tunnel due to the formation of an EDZ.

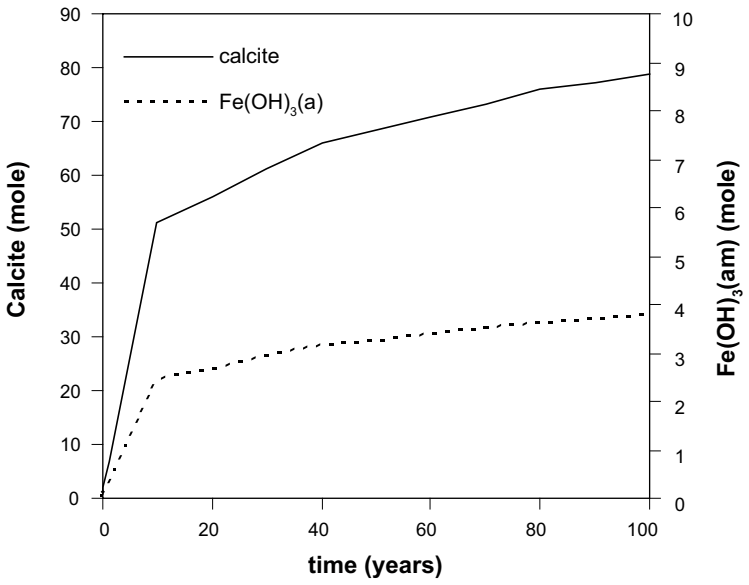

Figure 4-6. *Evolution of the amount of calcite and $Fe(OH)_3$ at the tunnel wall as a function of time.*

5 Sensitivity analysis in STAGE 1

In this section, we present the results of different sensitivity analysis of the modelling performed in order to evaluate the influence of other important factors that have not been included in the reference case reported in Chapter 4. In this case, we have conducted one additional simulation of the system in stage 1 to see the influence of considering different concentrations of aqueous Fe(II) in the groundwater.

We have not evaluated the dissolved O_2 consumption by microbially mediated organic matter oxidation given that as observed in the results of Chapter 4, $O_2(g)$ can not diffuse to the host rock due to the high flow velocity field. This reaction will be later evaluated in the sensitivity analyses of the stage 2 model.

5.1 The influence of the initial aqueous Fe(II) concentration in groundwater

The aqueous concentration of Fe(II) in water entering to the tunnel is another variable of interest that can exert an important control on the final mineral composition and groundwater composition near the tunnel wall.

In order to quantify this influence, we have considered different initial concentrations of iron in the groundwater, ranging from $5 \cdot 10^{-9}$ to $3 \cdot 10^{-3}$ mole dm^{-3}, being $3.3 \cdot 10^{-5}$ mole dm^{-3} the original value in the groundwater.

As in the reference case model (Chapter 4) the initial pore water in the fracture has been obtained by equilibrating the modified groundwater (with the corresponding Fe(II) concentration) with calcite and pyrite. The final composition has also been used as boundary groundwater. This has implied minor changes, mainly in the pH and in the redox potential (Table 5-1).

In Figure 5-1 we have plotted the final values of pH obtained at the tunnel wall (X = 17 m, Z = 20 m) at the end of the operational phase (time = 100 years), as well as the evolution of the amount of calcite and $Fe(OH)_3(am)$ precipitated at the tunnel wall.

As can be seen, in those conditions where calcite precipitates, pH is buffered to values near 7.7. In these cases, $Fe(OH)_3(am)$ also precipitates and thus, the behaviour is similar to the reference case as described in Section 4.2.7 and Figure 4-4.

Table 5-1. pH and redox potentials for initial fracture pore water and boundary groundwater obtained after equilibrating Forsmark groundwater (with modified [Fe(II)]) with calcite and pyrite.

[Fe(II)] (mole dm^{-3})	pH	pe	Eh(mV)
$5.0 \cdot 10^{-9}$	7.06	–3.0	–171.5
$3.3 \cdot 10^{-6}$	7.06	–2.8	–160.0
$3.3 \cdot 10^{-5}$	7.06	–2.7	–155.9
$3.3 \cdot 10^{-4}$	7.06	–2.7	–152.0
$6.0 \cdot 10^{-4}$	7.07	–2.6	–151.1
$1.0 \cdot 10^{-3}$	7.07	–2.6	–150.5
$3.3 \cdot 10^{-3}$	7.09	–2.6	–149.9

However, when the initial aqueous Fe(II) concentration is higher than $6.0 \cdot 10^{-4}$ mole dm^{-3}, the precipitation of $Fe(OH)_3(am)$ is very high causing a significant increase of the acidity of the system, see Equation 6. Under these conditions, calcite dissolves to buffer pH until it is exhausted, the pH value is not buffered anymore and reaches values of around 3.

Nevertheless, values of aqueous Fe(II) concentration higher than $6.0 \cdot 10^{-4}$ mole dm^{-3} are not expected to occur in the groundwaters given that, as observed in Figure 5-2 (grey circle), Fe^{2+} is not stable in solution and precipitates as siderite.

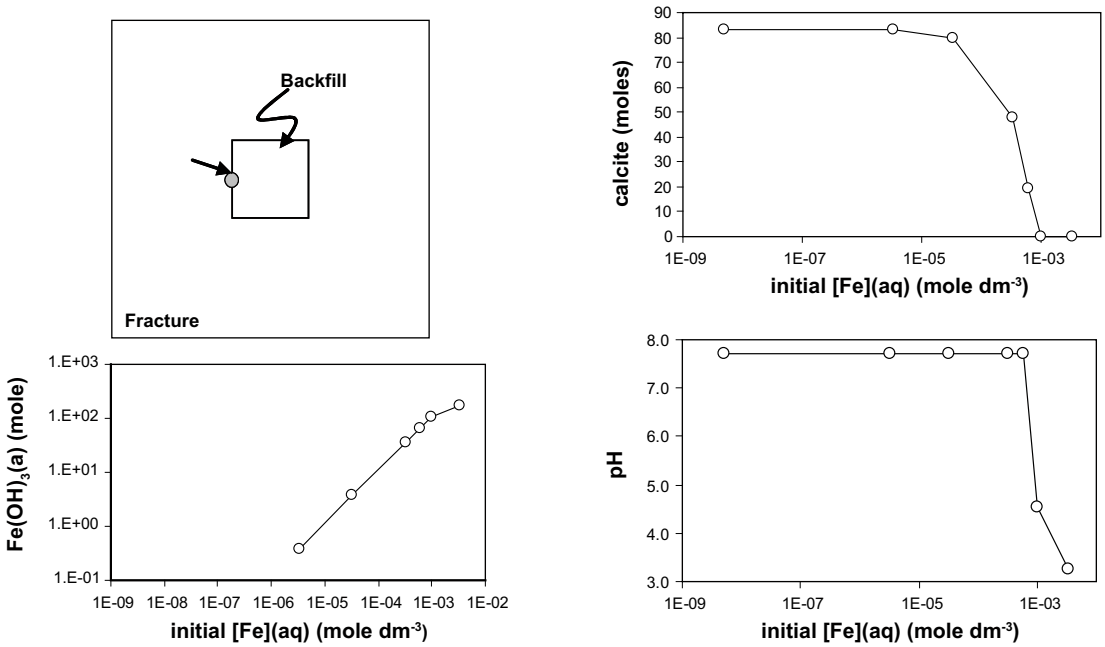

Figure 5-1. *Total amount of calcite and $Fe(OH)_3(am)$ precipitated at the tunnel wall and pH of groundwater in equilibrium with these minerals as a function of the initial [Fe(II)] of groundwater at the end of the operational phase (time = 100 years).*

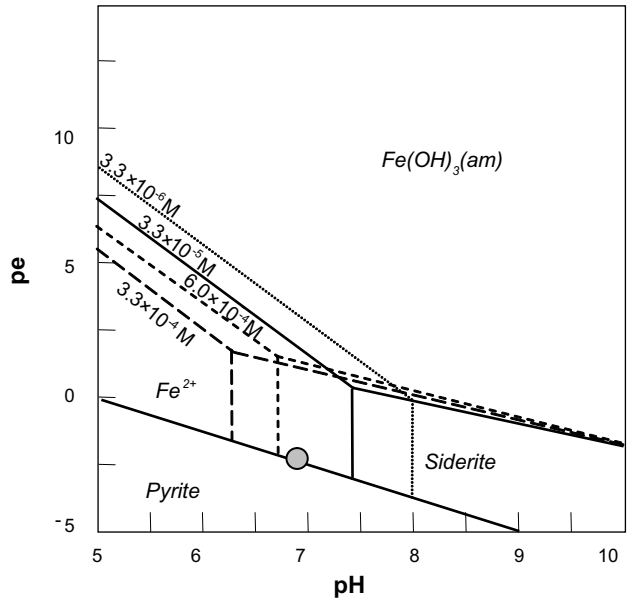

Figure 5-2. *Predominance area diagram of the Fe^{2+} system under the conditions of the fracture system (pe = Eh(mV)/0.2T). $pCO_2(g) = -2.21$, [S] = $5.2 \cdot 10^{-3}$M, [Ca] = $2.3 \cdot 10^{-2}$M. [Fe] varying from $3.3 \cdot 10^{-6}$ M to $3.3 \cdot 10^{-5}$M. The grey circle indicates the conditions of the initial groundwater considered for high [Fe].*

6 STAGE 2. Modelling of the post-operational phase

6.1 Conceptual model

6.1.1 Modelled domain and hydrodynamic system

There are two main differences related to the modelled domain and hydrodynamic system with respect to the model of stage 1.

a) The tunnel now is filled with a water saturated backfill.

b) The hydraulic regime is assumed to be governed by a regional gradient and water flows through the whole domain from left to right (Figure 6-1).

The model will be run for 60,000 years in order to simulate its long-term evolution.

6.1.2 Mineralogical and chemical system

As stated in the Sr-Can Safety Assessment, two different backfill concepts are analysed: the mixture and the clay concepts. In the mixture concept the entire section of the deposition tunnel is backfilled with an *in situ* compacted mixture of 70% of crushed rock and 30% of bentonite of the same type as the buffer (backfill 30/70). In the clay concept, the entire section of the deposition tunnel is completely backfilled with pre-compacted blocks of Friedland clay of about 0.25 m^3 of volume.

The potential materials included in these two backfill concepts are the MX-80 sodium bentonite from Wyoming, the Deponit CA-N calcium bentonite from Milos, the natural Friedland Clay and the crushed rock from the site.

In the calculations presented here the clay chosen either for the 30/70 mixture concept as well as for the clay concept is the MX-80 bentonite, given that it is the best characterized bentonite from a compositional, chemical and mineralogical point of view. The mineralogical composition of the 30/70 backfill and of the MX-80 bentonite is listed in Table 6-1. We have not included the

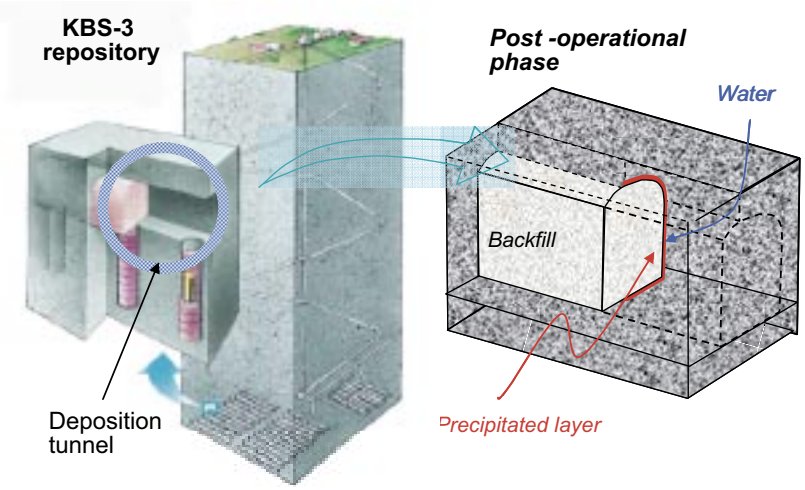

Figure 6-1. *Drawing of the conceptual model of the post-operational phase. The tunnel is now filled with water saturated backfill and water entering to the system crosses the oxidised layer formed during the operational phase.*

Friedland bentonite in the modelling given that we have not found information about its surface and/or exchange composition, except that the CEC is 0.22 eq kg^{-1} /SKB Interim report 2005/. Its mineralogical composition is available and shown in Table 6-1 for the sake of comparison.

The exchange capacity of the mixture is given by the bentonite component (Table 6-2) and the surface acidity will be only considered in the bentonite fraction of the backfill. The exchange coefficients (following the Gaines-Thomas convention) given in /Bradbury and Baeyens 2002/ have been used, while the acidity surface reactions constants are those reported in /Wersin 2003/ (Table 6-3).

In this stage 2 model, we assume that $O_2(g)$ present in the backfill has been consumed /see Grandia et al. 2006/. The mineralogical and chemical characteristics of the fracture plane are the same than those reported in Section 4.1.2. The main difference is that the intersection of the fracture in contact with the tunnel has a new mineral composition, according to the results obtained from the modelling of stage 1. Given that the actual oxygen concentration at this point is uncertain, we have assumed that environment is initially oxidising. In the model, the $O_2(g)$ concentration obtained from the modelling of stage 1 has been considered (0.54 mole dm^{-3}water) although this value is surely an overestimation of this surface after the backfilling process.

Table 6-1. Mineral composition (% wt) of the backfill 30/70 with MX-80 bentonite. Mineral composition of Friedland bentonite /from SKB Interim report 2005/.

Component (wt-%)	Forsmark granite	MX-80	30/70 mixture (MX-80)	Friedland
Albite		3	0.9	3
Feldspars	25	0	17.5	
Calcite + Siderite		0	0	
Cristobalite		2	0.6	
Dolomite		0	0	
Gypsum + anhydrite		0.7	0.21	0.8
Mica		4	1.2	9
Illite			0	4
Montmorillonite		87	26.1	
Illite/Smectite mixed layer			0	44
Kaolinite			0	10
Pyrite		0.07	0.021	0.62
Quartz	36	3	26.1	28
Plagioclase	39		27.3	
C organic			0	0.6
CEC (meq/100 g)		75	22.5	22

Table 6-2. Exchange composition of the MX-80 /from SKB 2004b/.

Components	MX-80
CEC_{bulk} (eq kg^{-1})	0.75 ± 0.02
Na- (%)	72 ± 5
K- (%)	2 ± 1
Mg- (%)	8 ± 5
Ca- (%)	18 ± 5
$CEC_{clay\ fraction}$ (eq kg^{-1})	0.85

Table 6-3. Exchange and surface reactions considered in the model.

Exchange reactions Species	Reaction (a)	
NaX	$X^- + Na^+ = NaX$	$\log K_{eq} = 0.0$
KX	$X^- + K^+ = KX$	$\log K_{eq} = 0.60$
MgX_2	$2X^- + Mg^{2+} = MgX_2$	$\log K_{eq} = 0.34$
CaX_2	$2X^- + Ca^{2+} = CaX_2$	$\log K_{eq} = 0.41$
Surface reactions **Species**	**Reaction (b)**	
ZOH_2^+	$ZOH + H^+ = ZOH_2^+$	$\log K_{eq} = 4.5$
ZO^-	$ZOH = ZO^- + H^+$	$\log K_{eq} = -7.9$
YOH_2^+	$YOH + H^+ = YOH_2^+$	$\log K_{eq} = 6.0$
YO^-	$YOH = YO^- + H^+$	$\log K_{eq} = -10.5$

(a) Data from /Bradbury and Baeyens 2002/. (b) Data from /Wersin 2003/.

Formation of FeS, gypsum and $Fe(OH)_3(am)$ in those areas where they are not present as primary minerals is allowed.

As well as in stage 1 model, no silicate bearing minerals have been considered. There are few studies dealing with smectite dissolution under repository conditions. /Huertas et al. 2001/ studied the kinetics of dissolution of a smectite from Sierra de Níjar (Almería, SE Spain) in granitic groundwater. The dissolution rate of this mineral depends on pH and at pH < 8, it follows a rate as expressed in Equation 8, if montmorillonite is far from equilibrium.

$$r\left(\frac{mol}{m^2 s}\right) = 10^{-11.39}\left[H^+\right]^{0.34} \qquad \text{Equation 8}$$

However, montmorillonite, as well as quartz, is close to equilibrium with backfill pore water and its dissolution is not significant. Moreover, the inclusion of the aluminium-system in the calculations would considerably increase the complexity of the numerical modelling.

The main processes expected to occur in this model are the same presented in Section 4.1.2: i) dissolution and/or precipitation (if it is the case) in equilibrium with all primary minerals except pyrite in the fracture and backfill material, as its dissolution will be kinetically driven and precipitation of amorphous FeS in case of oversaturation; ii) cation exchange and surface acidity reactions in equilibrium in the smectite fraction of the backfill.

6.2 Numerical model

6.2.1 Code Capabilities and grid and time discretization

The code capabilities and the grid discretization are the same as those described in Section 4.2.1 and 4.2.2. However, the time length of the simulation is 60,000 years, with a time step varying from 0.1 to 100 years. The time length of the simulation has been selected on the basis that, as stated by climate modelling, groundwaters entering in the repository may change significantly during a glacial cycle.

6.2.2 Hydrodynamic properties

Hydraulic head gradients at repository depths are unknown at Forsmark. In the present study, a hydraulic head gradient of 0.005 m m^{-1} has been selected for the modelling, which is a typical gradient for fractured granites at this depth /SKB 1999/.

As stated previously in the conceptual model, three different zones have been considered: the fracture plane, the fracture in contact with the tunnel (tunnel wall) and the backfill. The tunnel wall is represented by a layer of 0.25 m width. Transmissivity values reported by /Hartley et al. 2004/ for the fracture network range from $9{\cdot}10^{-9}$ to $6{\cdot}10^{-7}$ m^2s^{-1}. By following the same approach as in stage 1, a value of hydraulic conductivity of $5{\cdot}10^{-7}$ m s^{-1} has been considered for the fracture zone and the tunnel wall, while for the backfill, a value of $5{\cdot}10^{-11}$ m s^{-1} has been considered /from Börgesson et al. 2004/.

In Table 6-4 we list the values used for the different hydrodynamic properties.

6.2.3 Chemical properties

The mineral and pore water composition of the fracture plane used in this stage 2 model are the same than in stage 1 and are described in Section 4.2.4. The initial mineral and pore water compositions are listed in Table 6-5, as well as the initial exchange and surface composition. Data for the initial pore water and mineral composition at the tunnel wall come from the results of the stage 1 modelling. Data for the initial backfill pore water has been obtained by equilibrating groundwater with backfill minerals. No information is available about the reactive area of pyrite in backfill. Thus, we have assumed a particle diameter for pyrite in bentonite of 1 μm, which gives a geometrical area of 1.2 m^2 g^{-1}.

Table 6-4. Values used for the hydrodynamic properties of the different media.

Property	Fracture plane	Tunnel wall	Backfill
Porosity (%)	20[(1)]	20[(1)]	36.3[(2)]
Hydraulic cond. (m s^{-1})	$5{\cdot}10^{-7}$[(3)]	$5{\cdot}10^{-7}$[(3)]	$5{\cdot}10^{-11}$[(2)]
Transmissivity (m^2s^{-1})	$2{\cdot}10^{-7}$		
Dispersivity (m)	From 0.01 to 0.001		
Diffusivity (m^2s^{-1})	$1.0{\cdot}10^{-10}$[(4)]		

[(1)] /Dershowitz et al. 2003/ [(2)] /Börgesson et al. 2004/ [(3)] /Hartley et al. 2004/ [(4)] /Ochs and Talerico 2004/.

Table 6-5. Initial water and mineral composition for the backfill and tunnel wall and fracture materials. Initial exchange and surface composition for backfill is also listed. Values in mole dm^{-3} water except for redox data and pH.

Components	Backfill	Tunnel wall	Fracture plane
pH	7.19	7.72	7.09
Eh(mV)	–157.5	783.8†	–148.3
Na	$1.71{\cdot}10^{-1}$	$8.90{\cdot}10^{-2}$	$8.90{\cdot}10^{-2}$
Ca	$1.78{\cdot}10^{-2}$	$2.23{\cdot}10^{-2}$	$2.30{\cdot}10^{-2}$
Mg	$5.70{\cdot}10^{-3}$	$9.30{\cdot}10^{-3}$	$9.30{\cdot}10^{-3}$
K	$1.60{\cdot}10^{-3}$	$9.00{\cdot}10^{-4}$	$9.00{\cdot}10^{-4}$
Fe	$3.30{\cdot}10^{-5}$	$1.24{\cdot}10^{-7}$	$3.30{\cdot}10^{-5}$
HCO_3^-	$2.19{\cdot}10^{-3}$	$4.58{\cdot}10^{-4}$	$2.15{\cdot}10^{-3}$
Cl^-	$1.53{\cdot}10^{-1}$	$1.53{\cdot}10^{-1}$	$1.53{\cdot}10^{-1}$
SO_4^{2-}	$3.78{\cdot}10^{-2}$	$5.20{\cdot}10^{-3}$	$5.20{\cdot}10^{-3}$
Si	$1.26{\cdot}10^{-4}$	$1.85{\cdot}10^{-4}$	$1.85{\cdot}10^{-4}$
Mineral			
Calcite	–	0.11	11.5
$Fe(OH)_3$(am)	–	$5.26{\cdot}10^{-3}$	–
Siderite	–	–	–
FeS(ppt)	–	–	–
Gypsum	$3.25{\cdot}10^{-2}$	–	–
Pyrite	$8.40{\cdot}10^{-3}$	–	0.04

Exchange species			
NaX	0.653	–	–
KX	0.023	–	–
MgX_2	0.038	–	–
CaX_2	0.138	–	–
Surface species (surface density 31.5 $m^2\ g^{-1}$).			
ZOH (tot)	0.060	–	–
YOH (tot)	0.057	–	–

†: the amount of dissolved oxygen in the tunnel wall water is: $[O_2] = 0.54$ mol L^{-1}.

6.2.4 Boundary and initial conditions

The model assumes that groundwater flows through the fracture plane from the left boundary to the right boundary. A prescribed hydraulic head has been imposed at both boundaries. A fixed solution composition has been imposed at the left boundary, whereas at the right boundary, the solution composition is allowed to change as a consequence of the chemical reactions considered. Upper and lower boundaries of the domain are no flow boundaries. Initial pore water and mineral composition have been previously presented in Section 6.2.3.

6.2.5 Results

The established boundary conditions force water to flow from the left to the right boundaries of the system (Figure 6-2). The groundwater flow at these boundaries is 0.006 $dm^3\ min^{-1}\ m^{-1}$.

The initial conditions of the groundwater in the fracture plane are reducing, given that it equilibrates with pyrite and calcite. Initially, the tunnel wall contains oxidising groundwater, equilibrated with calcite and $Fe(OH)_3$(am). The water in the backfill is reducing, equilibrated with pyrite.

Given that the hydraulic conductivity of the backfill material is lower than that of the fracture when water arrives to the tunnel, it tends to surround it, although a small diffusion front through the backfill develops.

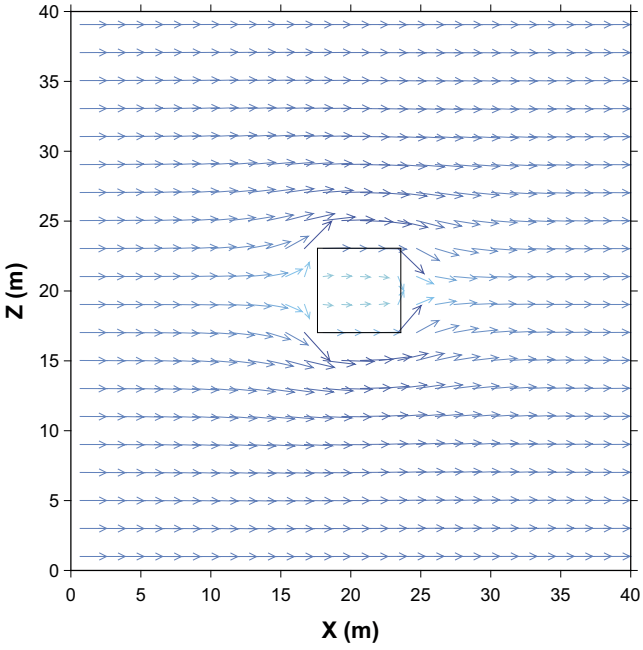

Figure 6-2. *Velocity field obtained by using the boundary conditions specified in Section 6.2.4.*

Water entering the backfill has flown through the oxidized layer and thus, it has a higher value of the redox potential (Figure 6-3). The evolution of dissolved O_2 is shown in Figure 6-4. This produces an increase of pyrite dissolution (Figure 6-5) and $Fe(OH)_3(am)$ precipitation (Figure 6-6), especially in the contact with the fracture.

Pyrite dissolution is not significant after the first 200 years. However, during this first time period, and given that pyrite in the backfill has a higher reactive surface area, this process is more important in the backfill than in the fracture area.

The value of the redox potential is directly related to the concentrations of aqueous Fe(II) and Fe(III) present in the backfill water.

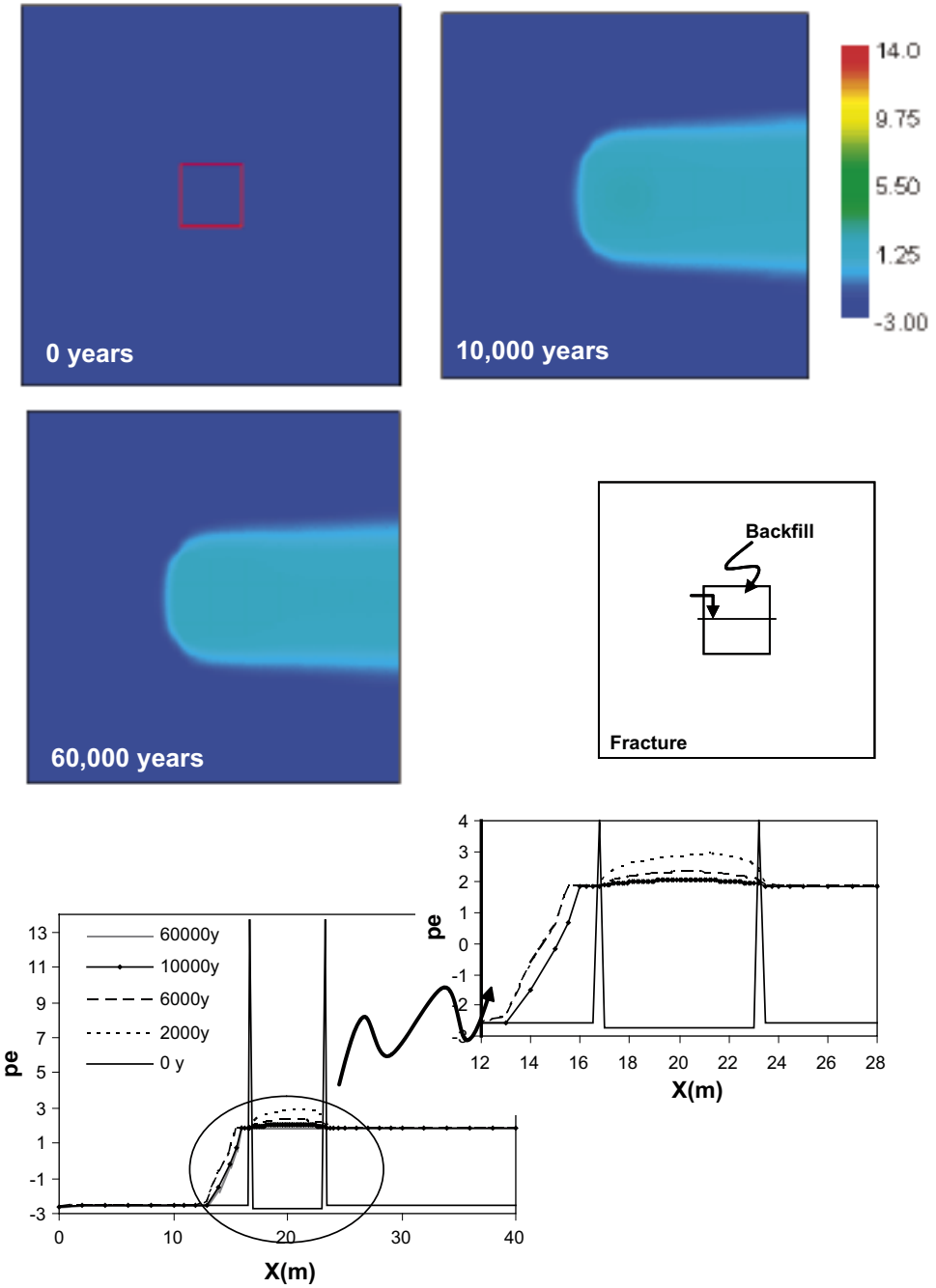

Figure 6-3. *Time evolution of the redox potential in terms of pe (pe = Eh(mV)/0.2T) in the modelled system and a detailed evolution of the redox potential at Z = 20 m.*

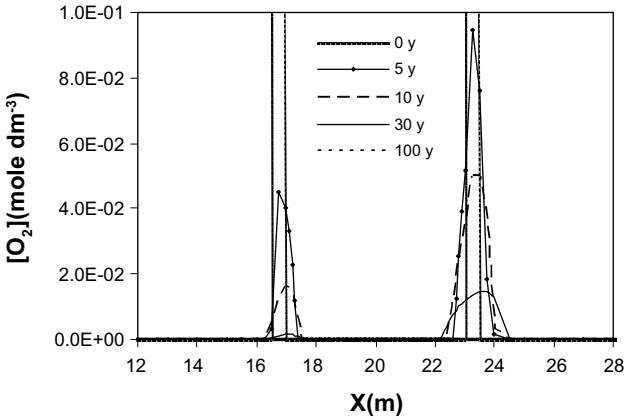

Figure 6-4. *Time evolution of O_2(aq) concentration (mole dm^{-3}) at Z = 20 m.*

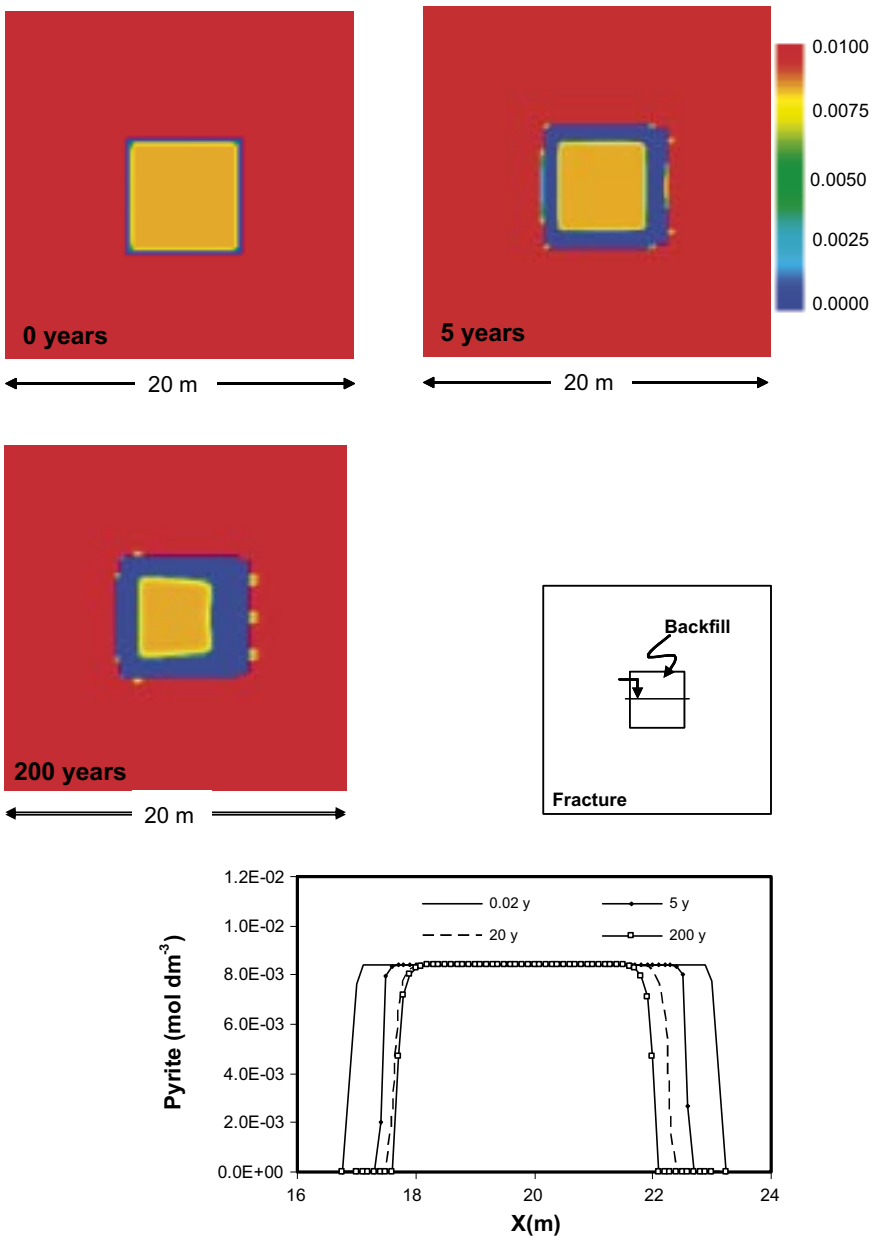

Figure 6-5. *Time evolution of pyrite in the modelled system and a detailed evolution of pyrite in the backfill at Z = 20 m. Values in mole dm^{-3} water.*

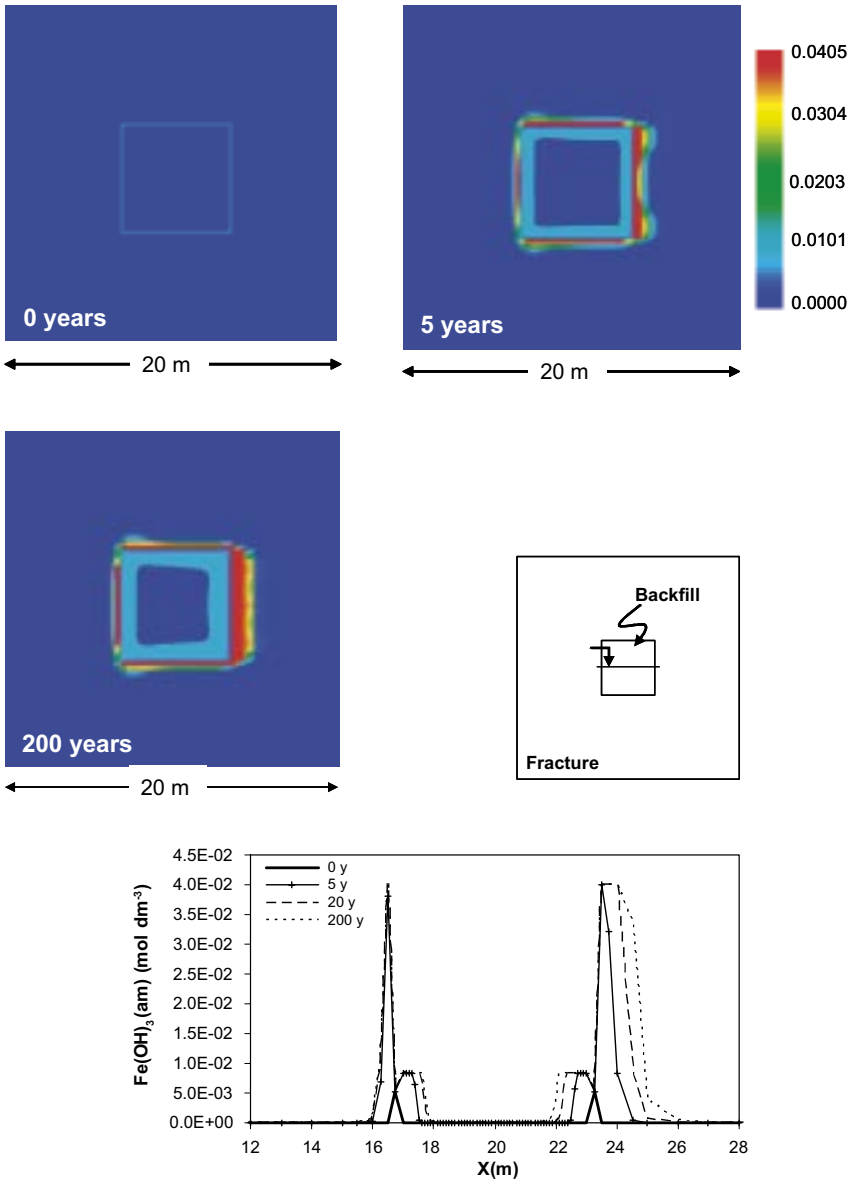

Figure 6-6. *Time evolution of $Fe(OH)_3(am)$ in the modelled system and a detailed evolution of $Fe(OH)_3(am)$ in the backfill at Z = 20 m. Values in mole dm^{-3} water.*

In the predominance area diagram plotted in Figure 6-7 we have drawn the evolution of the redox potential and Fe aqueous concentration evolution as a function of time in the tunnel wall area and in the backfill close to it. It can be seen in Figure 6-7a how the water in the tunnel wall evolves from high redox potential and low Fe concentration, determined by the Fe(III)/$Fe(OH)_3(am)$ equilibrium to more reductive and with higher Fe concentration, determined by the Fe(II)/$Fe(OH)_3(am)$ equilibrium.

In Figure 6-7b, we present the same evolution but in the backfill near the fracture. Initially, pore water is in equilibrium with pyrite, but as soon as oxidising groundwater enters into the backfill pyrite is not stable anymore. $Fe(OH)_3(am)$ starts to precipitate and pH decreases down to 5.5. Then, the pH starts to recover and at the end, we can observe the same evolution than in the tunnel wall: the redox potential is controlled by the equilibrium Fe(II)/$Fe(OH)_3(am)$.

Groundwater entering the backfill is not saturated with gypsum. However, given its higher Ca concentration and the presence of sulphate generated by the oxidation of pyrite in the backfill, gypsum precipitates in the backfill near the tunnel wall during the first 2 to 5 years. When no more sulphate is generated by pyrite dissolution, gypsum starts to dissolve and it is completely

removed from the backfill before 1,000 years (Figure 6-8). The concentration of Ca in the inflowing water is higher than in the backfill, what produces calcite precipitation, especially at the contact with the tunnel wall, and an increase of exchanged Ca in bentonite (Figure 6-9).

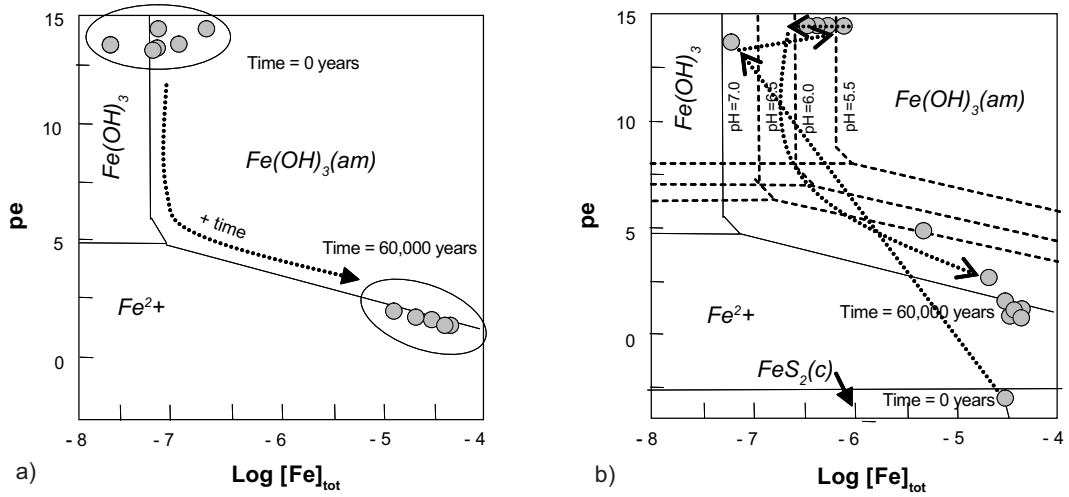

Figure 6-7. *Predominance area diagrams of water at the tunnel-backfill boundary (pe = Eh(mV)/0.2T). T = 15°C. a) Tunnel wall. pH = 7.0 $[C]_{tot}$ = 2.1·10⁻³M, [S] = 5.2·10⁻³M, [Ca] = 2.3·10⁻³M. b) Backfill in contact with the tunnel wall (X = 17.0, Z = 20.0 m). pH = 5.5 to 7.0 $[C]_{tot}$ = 2.1·10⁻³M, [S] = 5.2·10⁻³M, [Ca] = 2.3·10⁻³M. Grey circles are values given by the model at different times at the selected points.*

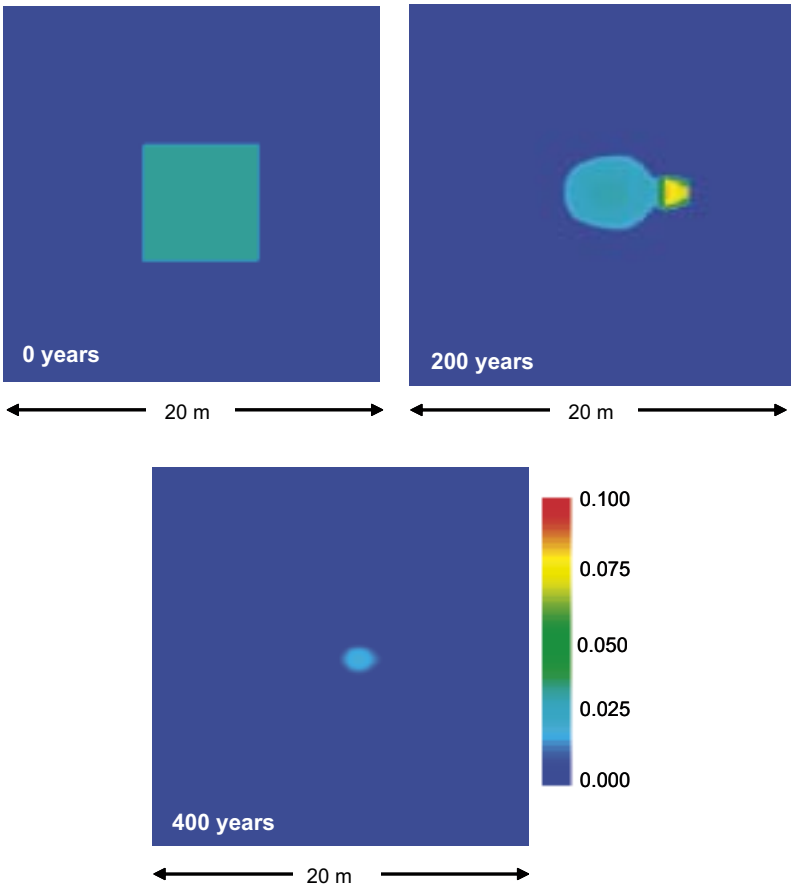

Figure 6-8. *Time evolution of gypsum in the modelled system. Concentrations in mole dm⁻³ water.*

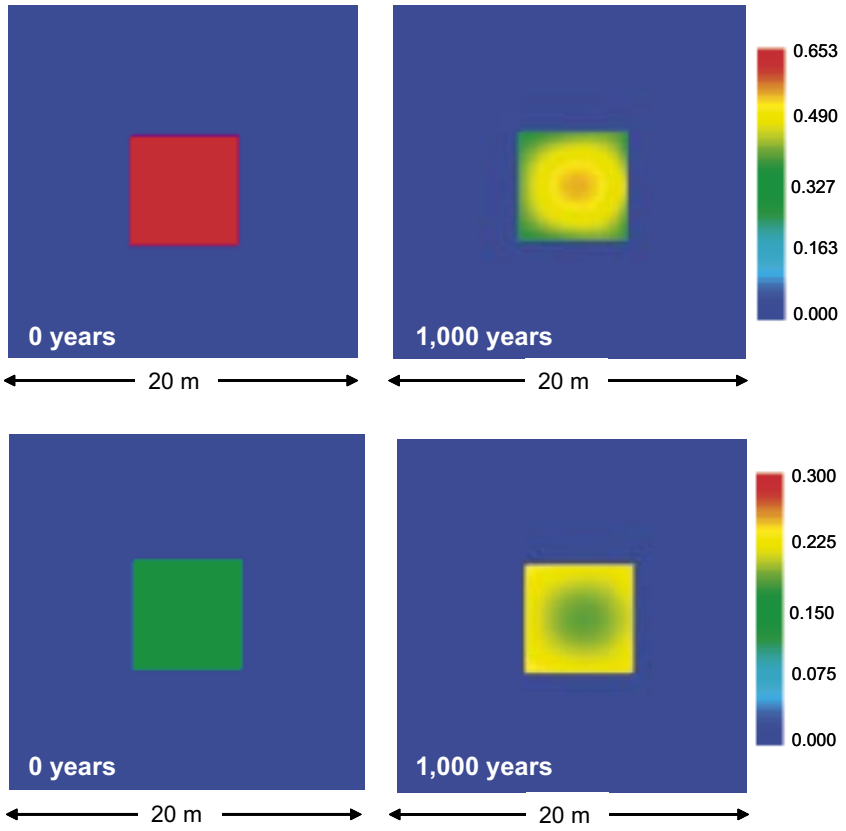

Figure 6-9. *Time evolution of NaX (upper plots) and CaX_2 (lower plots) in mole dm^{-3} water.*

As in the case of Ca, the aqueous concentration of Mg is higher in water entering the tunnel than in the backfill water. As a consequence, the Mg occupancy in the exchanger increases. In contrast, the aqueous concentration of Na and K in water entering the system is lower than initial backfill pore water. Consequently, the concentration of NaX and KX species decrease (Figure 6-9). The final concentrations of exchanged species are listed in Table 6-6 for comparison.

The dissolution of pyrite and precipitation of $Fe(OH)_3(am)$ in the backfill and the precipitation of calcite increases the acidity of the media according to Equation 9 and Equation 10.

$$FeS_2\,(s) + 3.75\,O_2\,(aq) + 3.5\,H_2O \rightarrow Fe(OH)_3\,(am) + 2\,SO_4^{2-} + 4H^+ \qquad \text{Equation 9}$$

$$Ca^{2+} + HCO_3^- = CaCO_3 + H^+ \qquad \text{Equation 10}$$

The results of the model show a significant decrease of pH down to 5.5 in the area of the backfill in contact with the tunnel. This decrease is only observed during the first 100 years of simulation and it is mainly due to the dissolution of pyrite and precipitation of $Fe(OH)_3(am)$, occurring during this time. However, the speciation of the surface species of MX-80 changes

Table 6-6. Initial and final exchange composition of backfill.

Species	Mole·dm^{-3} of water		% over total CEC	
	0 y	60,000 y	0 y	60,000 y
NaX	0.653	0.35	63%	34%
KX	0.023	0.014	2%	1%
MgX2	0.038	0.09	7%	18%
CaX2	0.138	0.243	27%	47%

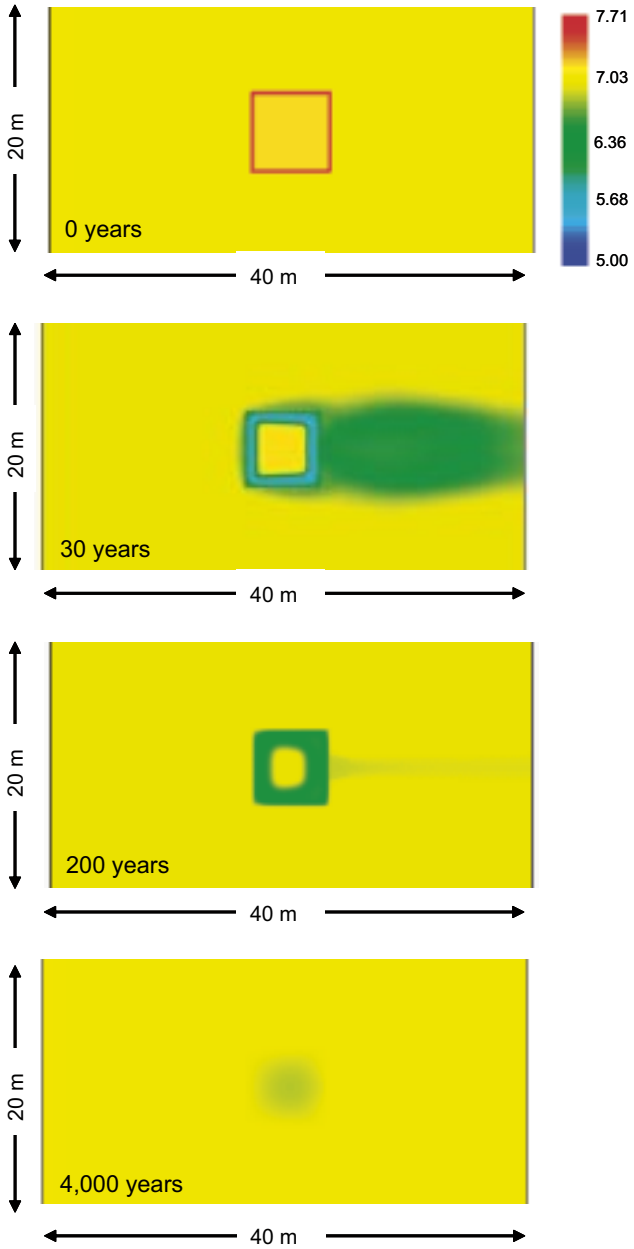

Figure 6-10. *Time evolution of pH.*

with time, showing an increase of the acidic component, suggesting that the acidity generated by the dissolution of pyrite and precipitation of $Fe(OH)_3(am)$ is partially buffered by the formation of ZOH_2^+ and YOH_2^+ on the clay surface. After the first 100 years, pH is again around 7 and minor changes are observed. After 2,000 years it can be considered constant and equal to the pH of the groundwater (Figure 6-10), and no important changes are observed when calcite precipitates in the backfill at 30,000 years.

The decrease of pH would affect the dissolution of carbonates and aluminosilicates. Nevertheless, the presence of carbonates in the backfill, as we will see, would prevent the pH value to decrease to values as low as in this case.

In the absence of carbonates, the low pH values would disappear for times longer than 30 years. Within this time period, the lowest pH value achieved in the system (pH = 5.4) would imply a maximum dissolution of 10^{-7} moles dm^{-3} water of aluminosilicate, which would not affect the major properties of the system studied.

7 Sensitivity analysis in STAGE 2

As in the Stage 1 model, we present in this section the results of different sensitivity analysis of the modelling performed in order to evaluate the possible uncertainties in the reference case reported in Chapter 6.

In this case, we have conducted 4 additional simulations of the stage 2 model, which can be briefly described as following:

1) Inclusion of 0.7% wt of calcite in the initial MX-80 composition, to evaluate the influence of carbonate minerals of bentonite in the overall behaviour of the backfill system.
2) Inclusion of 0.7% wt of siderite in the initial MX-80 composition. As in the previous case, the aim is to assess the influence of carbonate minerals of bentonite in the overall behaviour of the backfill system, but siderite is of special interest because it is a Fe(II)-bearing carbonate and can exert a control on the redox state of the system.
3) Evaluation of the influence of initial amount of $Fe(OH)_3(am)$ formed in the oxidised zone in the backfill behaviour.
4) Inclusion of the organic matter oxidation due to the presence of microbial activity, as an oxygen consumer reaction.

7.1 Calcite

One of the uncertainties reported in /SKB 2004b/ related to the mineralogical composition of bentonite MX-80 is the content of carbonate minerals of this bentonite. The final value accepted and given in /SKB 2004b/ is that the amount of calcite in bentonite is 0 ± 1% wt.

In this section we have tested the influence on the overall system of an initial value of calcite in bentonite of 0.7% wt as reported in /Madsen 1998/. Taking into account that in our conceptual model the backfill is of the type 30/70 mixture, this amount of calcite is equivalent to a concentration of 0.10 mole of calcite per dm^3 of water.

Initially, this variation only affects the mineral composition of backfill, and thus the initial water and exchange composition of backfill, although only minor changes have been produced (Table 7-1).

From the results obtained it can be said that the presence of an initial amount of calcite in backfill slightly modifies the behaviour of the system as reported for the previous base case.

Pyrite is dissolved in the backfill because the oxidant water in equilibrium with $Fe(OH)_3(am)$ of the tunnel wall is flowing through the backfill area. As in the previous case, pyrite only dissolves during the first 200 years, and then no more dissolution is observed. At the same time, $Fe(OH)_3(am)$ precipitates.

pH decreases, as observed in the base case, but it does not achieve values as low as 5.5 near the tunnel wall, given that the presence of calcite buffers the acidity generated by the oxidation of pyrite. The lowest pH value observed is around 6 after 5 years (Figure 7-1). pH achieves the value of Forsmark groundwater at shorter times than in the base case.

Table 7-1. Initial pore water, mineral, exchange and surface composition for the backfill obtained after equilibrating groundwater with new backfill mineral composition. Values in mole dm^{-3} water except for the case of redox potential and pH.

Components	Backfill
pH	7.22
pe	–2.8
Eh(mV)	–159.4
Na	$1.71 \cdot 10^{-1}$
Ca	$1.80 \cdot 10^{-2}$
Mg	$5.71 \cdot 10^{-3}$
K	$1.59 \cdot 10^{-3}$
Fe	$3.30 \cdot 10^{-5}$
HCO_3^-	$2.60 \cdot 10^{-3}$
Cl^-	$1.53 \cdot 10^{-1}$
SO_4^{2-}	$3.77 \cdot 10^{-2}$
Si	$1.26 \cdot 10^{-4}$
Mineral	
Calcite	0.10
$Fe(OH)_3$(am)	–
Siderite	–
FeS(ppt)	–
Gypsum	$3.25 \cdot 10^{-2}$
Pyrite	$8.40 \cdot 10^{-3}$
Exchange species	
NaX	0.653
KX	0.023
MgX_2	0.038
CaX_2	0.138

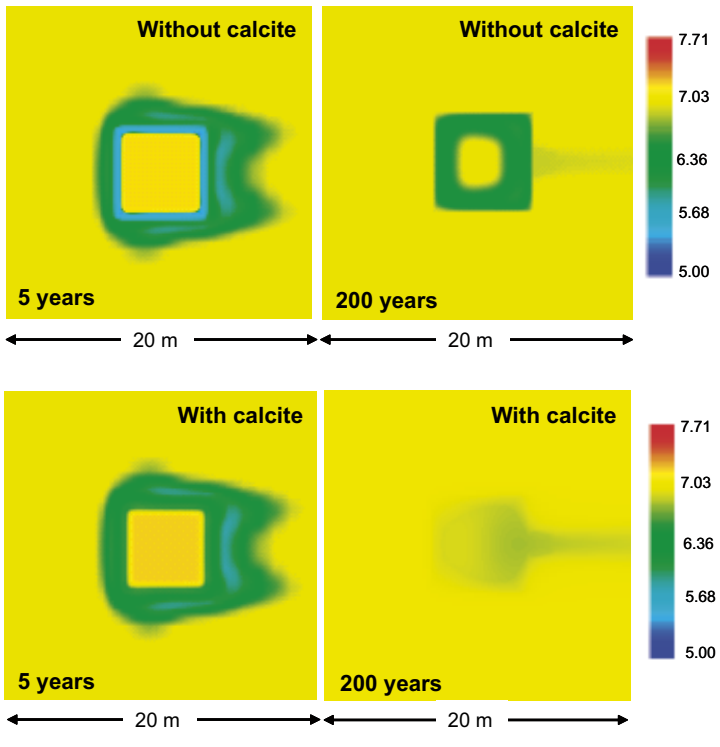

Figure 7-1. *Time evolution of pH in the base case (upper diagrams) and when 0.7% wt of calcite in bentonite is considered (lower diagrams).*

The buffering effect of calcite (Figure 7-2) is especially observed near the tunnel wall.

Dissolution of calcite also causes an increase of [Ca] in solution that precipitates as gypsum. The precipitation of gypsum is important near the tunnel wall and it reaches a maximum between 2 and 5 years, due to the enhanced dissolution of calcite (source of Ca) induced by the acidity generated by the dissolution of pyrite. However, after this period of time gypsum dissolves and after 200 years (when the source of sulphate is also exhausted) no more gypsum is found in the backfill.

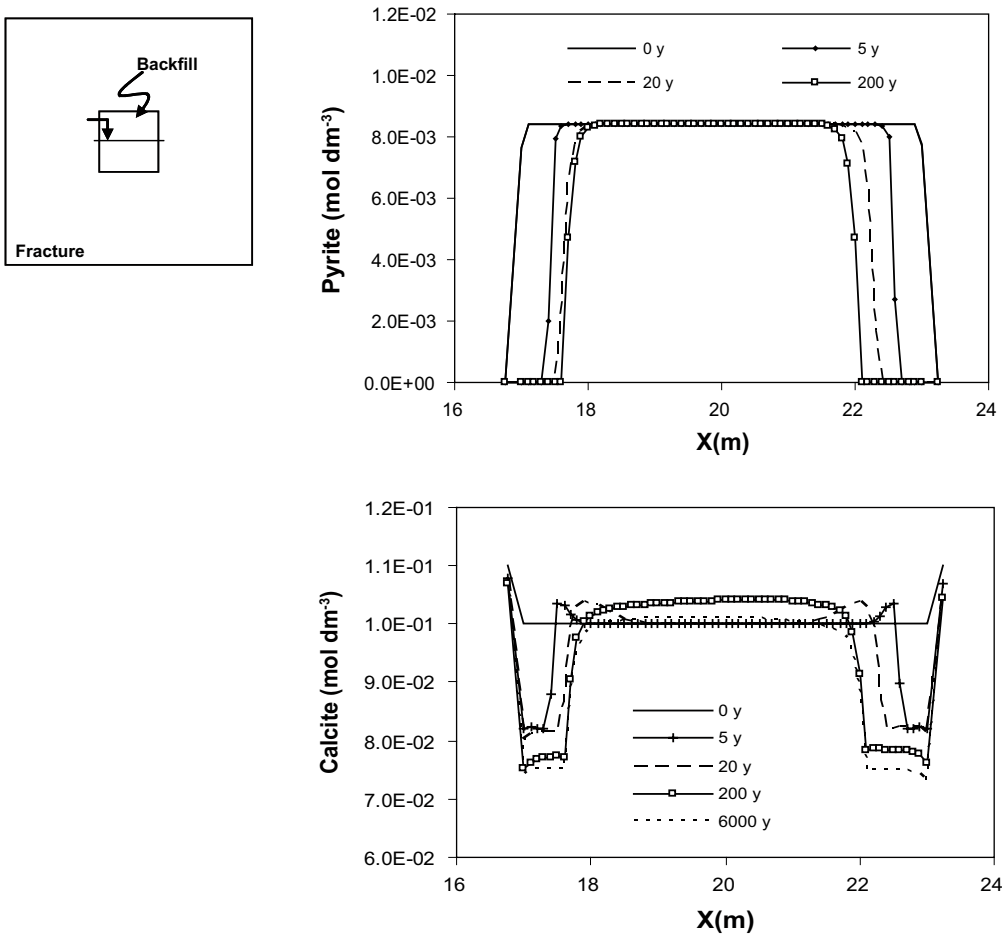

Figure 7-2. *Detailed evolution of pyrite and calcite in the backfill at Z = 20 m.*

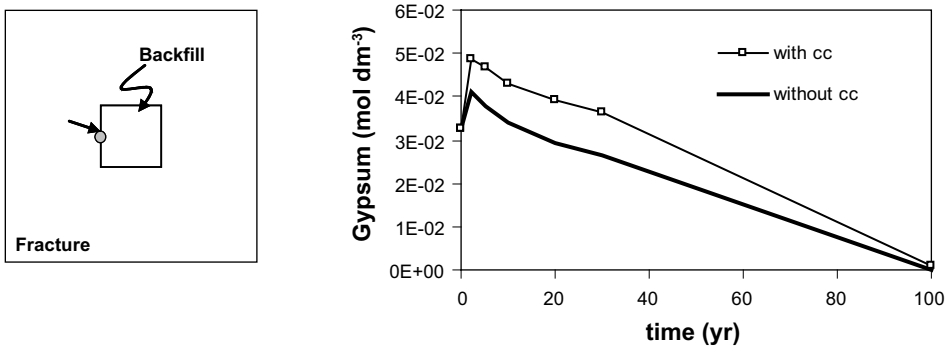

Figure 7-3. *Evolution of gypsum precipitated in the backfill (near the tunnel wall, X = 17.1 m, Z = 20 m) as function of time.*

7.2 Siderite

As in the case of calcite, the amount of siderite in the bentonite component of the backfill is another of the uncertainties identified in these calculations. /Madsen 1998/ reported a total of 1.4% wt of carbonates (siderite + calcite) in his analyses of MX-80 bentonite. In this case, we have considered an amount of 0.7% wt of siderite in order to assess the influence of this mineral on the system. Taking into account that in our conceptual model the backfill is of the type 30/70 mixture, this amount of siderite is equivalent to a concentration of 0.086 moles siderite per dm^3 of water.

Given that the modelled period is of 60,000 years and that siderite dissolution can be considered as a process of fast kinetics, we have assumed that siderite dissolves in equilibrium instead of following the kinetic law reported in /Grandia et al. 2006/.

Initially, the inclusion of siderite in the system only affects very slightly to the mineral composition of the backfill, and thus to its initial pore water and exchange composition (see Table 7-2).

As in the base case reported in Section 6.2, water entering the backfill has a higher redox potential due to its interaction with the more oxidised tunnel wall surface minerals formed during stage 1. In the base case this fact promoted the oxidation of pyrite following Equation 9. In this case, the postulated initial amount of oxygen causes the dissolution of siderite (Equation 11) and the consequent precipitation of iron as $Fe(OH)_3(am)$.

$$FeCO_3(s) + 0.25\ O_2 + 2.5\ H_2O = Fe(OH)_3(am) + HCO_3^- + H^+ \qquad \text{Equation 11}$$

Table 7-2. Initial pore water, mineral, exchange and surface composition for the backfill obtained after equilibrating groundwater with new backfill mineral composition. Values in mole dm^{-3} water except for the case of redox potential and pH.

Components	Backfill
pH	7.191
pe	–2.73
Eh (mV)	–156.0
Na	$1.71 \cdot 10^{-1}$
Ca	$1.79 \cdot 10^{-2}$
Mg	$5.70 \cdot 10^{-3}$
K	$1.59 \cdot 10^{-3}$
Fe	$8.94 \cdot 10^{-5}$
HCO_3^-	$2.54 \cdot 10^{-3}$
Cl^-	$1.53 \cdot 10^{-1}$
SO_4^{2-}	$3.79 \cdot 10^{-2}$
Si	$1.26 \cdot 10^{-4}$
Mineral	
Calcite	–
$Fe(OH)_3(am)$	–
Siderite	$8.66 \cdot 10^{-2}$
FeS(ppt)	–
Gypsum	$3.25 \cdot 10^{-2}$
Pyrite	$8.40 \cdot 10^{-3}$
Exchange species	
NaX	0.653
KX	0.023
MgX_2	0.038
CaX_2	0.138

In this case, both processes, oxidation of pyrite and of siderite contribute to the oxygen consumption and therefore, the reaction front is somewhat slower than in the base case. Because of that, when siderite is present in the system, less pyrite is oxidised after 60,000 years. This is reflected in Figure 7-4 and Figure 7-5, where we have plotted the amount of pyrite that remains in the backfill after 60,000 years for the base case and for the case studied in this section.

In the same way, in Figure 7-6 we have plotted the evolution of the amount of siderite present in the backfill and as it can be seen when comparing Figure 7-5 and Figure 7-6, after 60,000 years, the dissolution front coincides with the dissolution front of pyrite.

The dissolution of siderite causes an increase of the total amount of iron in the pore water, which in turn precipitates as $Fe(OH)_3(am)$ increasing the acidity of the system. In Figure 7-7, we have plotted the amount of aqueous Fe in the pore water and it can be seen how it increases due to the dissolution of siderite, while in the base case, this increase is not observed.

Thus, the presence of siderite in the system causes a larger precipitation of $Fe(OH)_3(am)$ (Figure 7-8) and a higher decrease of pH (Figure 7-9).

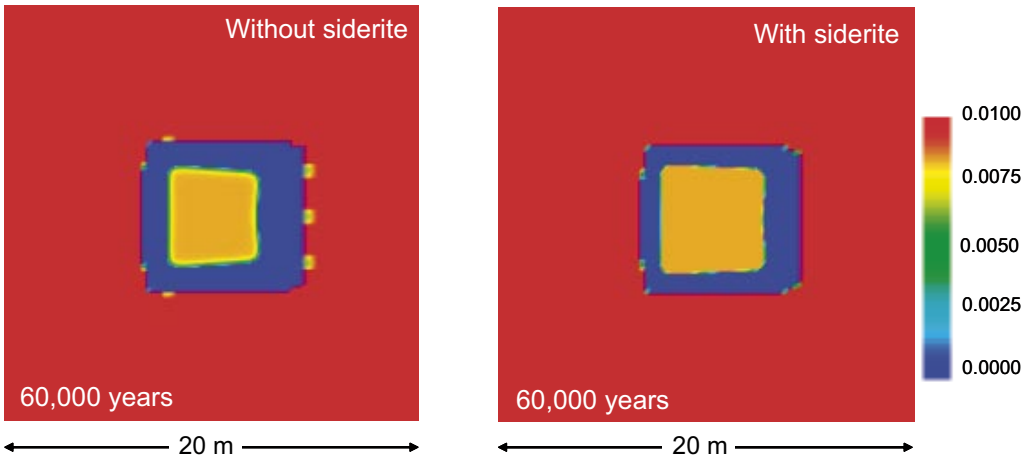

Figure 7-4. *Amount of pyrite remaining in the backfill system after 60,000 years for the base case (left diagram) and for the case considering 0.7% wt siderite (right diagram). Values in mole dm^{-3} water.*

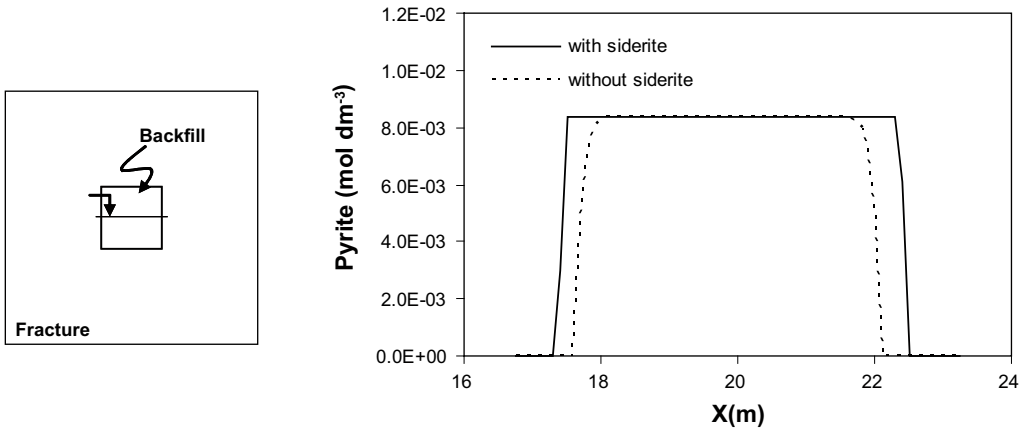

Figure 7-5. *Detail of the amount of pyrite remaining in the backfill system after 60,000 years for the base case (dashed line) and for the case considering 0.7% wt siderite (continuous line) (Z = 20 m).*

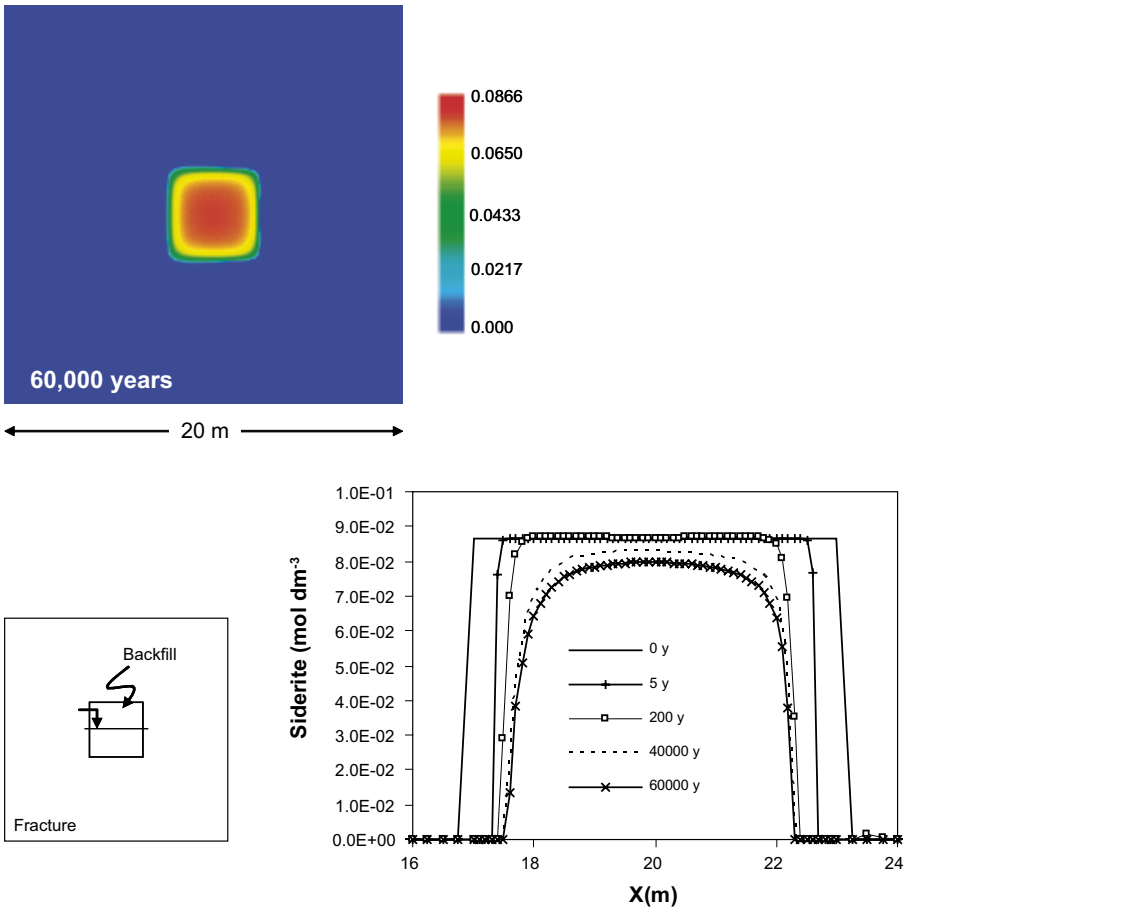

Figure 7-6. *Amount of siderite remaining in the backfill system after 60,000 years (upper diagram). Detailed evolution of siderite as a function of time at Z = 20 m (lower diagram). Values in mole dm^{-3} water.*

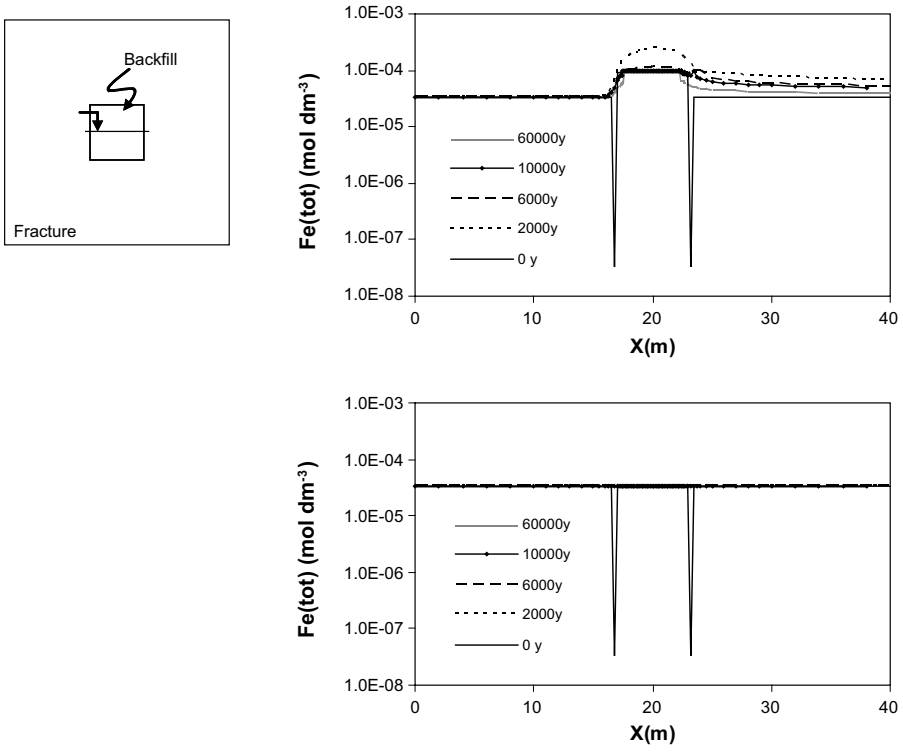

Figure 7-7. *Detail of the aqueous iron concentration evolution as a function of time at Z = 20 m. Lower diagram: base case (without siderite); upper diagram: with siderite.*

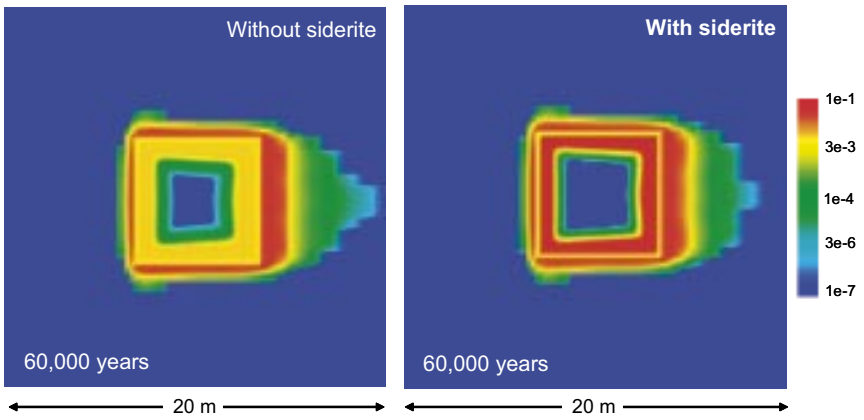

Figure 7-8. *Amount of $Fe(OH)_3(am)$ precipitated in the backfill system as the result of siderite and pyrite dissolution at time = 60,000 years for the base case (left diagram) and the case with siderite (right diagram). Values in mole dm^{-3} water.*

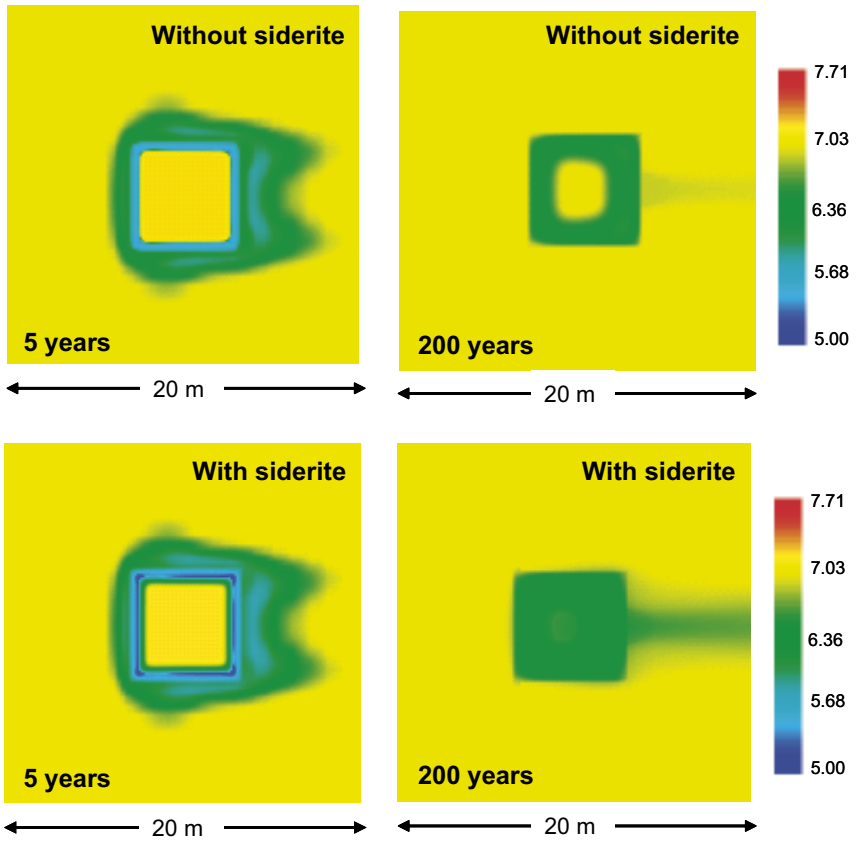

Figure 7-9. *pH evolution of the system in the base case (upper diagrams) and in the case with siderite (lower diagrams).*

However, as dissolution of siderite competes with dissolution of pyrite, the system reaches a stationary state sooner than in the base case and after 30–100 years of postoperational phase, no significant dissolution of both minerals is observed. In the base case, this was observed after 200 years.

Dissolution of siderite also causes an increase of aqueous carbonate. But calcite can not precipitate because of the low pH resulting from the precipitation of $Fe(OH)_3(am)$. When pH recovers after 100 years of postoperational phase, precipitation of calcite is significant near the tunnel wall, in those areas where siderite and pyrite have been totally dissolved (Figure 7-10). The amount of calcite precipitated is considerably higher than in the base case (Figure 7-11).

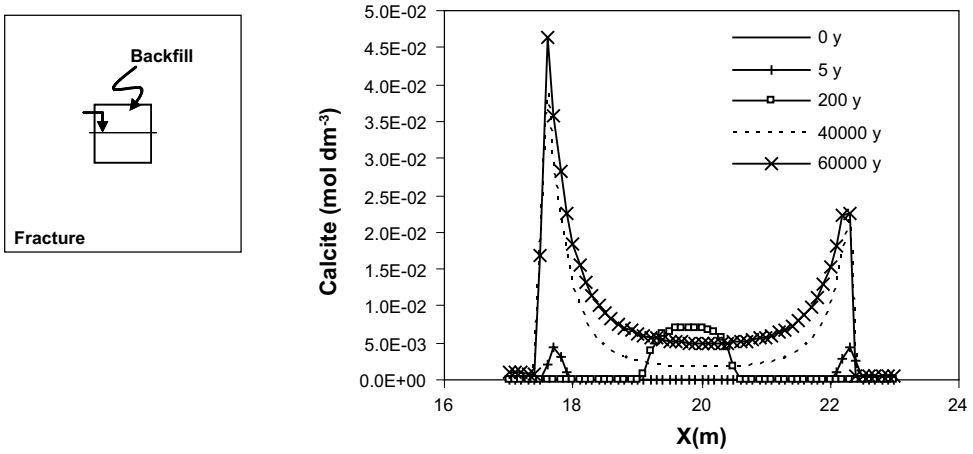

Figure 7-10. *Detailed evolution of calcite precipitated in the backfill as a function of X(m) for different times at Z = 20 m (right diagram).*

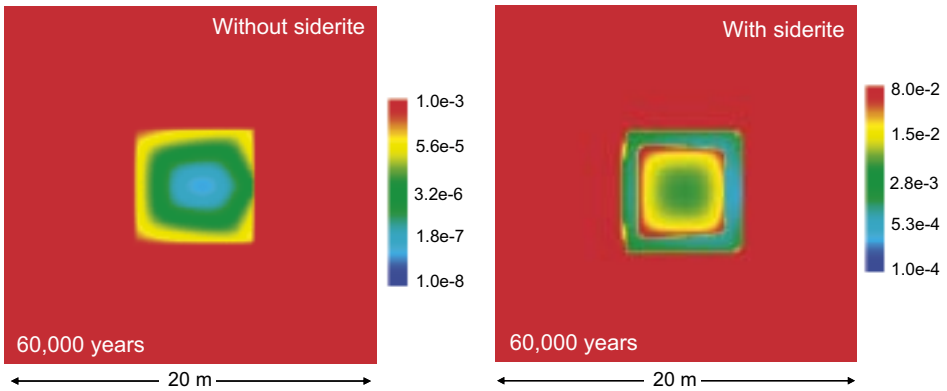

Figure 7-11. *Amount of calcite in the system at time = 60,000 years for the base case (left diagram) and the case considering siderite (right diagram). Values in mole dm^{-3} water. Note the difference in scale of concentration.*

Most changes are observed during the first 100 years. After that, and as in the base case after 200 years, a stationary state governed by the equilibrium of minerals and Forsmark groundwater is imposed. Calculated values of pH and cation and anion concentrations are those of Forsmark groundwater and exchange and surface concentrations are the same in both cases. In the case of considering siderite in the backfill the redox potential obtained at this stationary state is slightly lower than in the base case, which is pe = 1.4 (Eh = 80.0 mV) instead of 1.8 (Eh = 102.9 mV).

As in the base case, the redox control is thus exerted by the Fe system. In the tunnel wall the evolution of the redox potential is the same than reported in the base case. From a highly oxidised groundwater (due to the high O_2(g) concentration) where $Fe(OH)_3$(am) was in equilibrium with Fe(III) aqueous species, waters evolve to a less oxidising system where redox potential is controlled by the equilibrium $Fe(OH)_3$(am)/Fe(II) aqueous species (Figure 7-12).

However, in the backfill, where the initial groundwater is in equilibrium with siderite and pyrite (Figure 7-12), the contact with a more oxidising groundwater produces an increase of the redox potential which is controlled by the equilibrium siderite/$Fe(OH)_3$(am) until siderite is totally dissolved. At this point waters evolve to more oxidising and with time their redox potential evolve as in the tunnel wall, to waters with a redox potential controlled by the equilibrium Fe(II)/$Fe(OH)_3$(am).

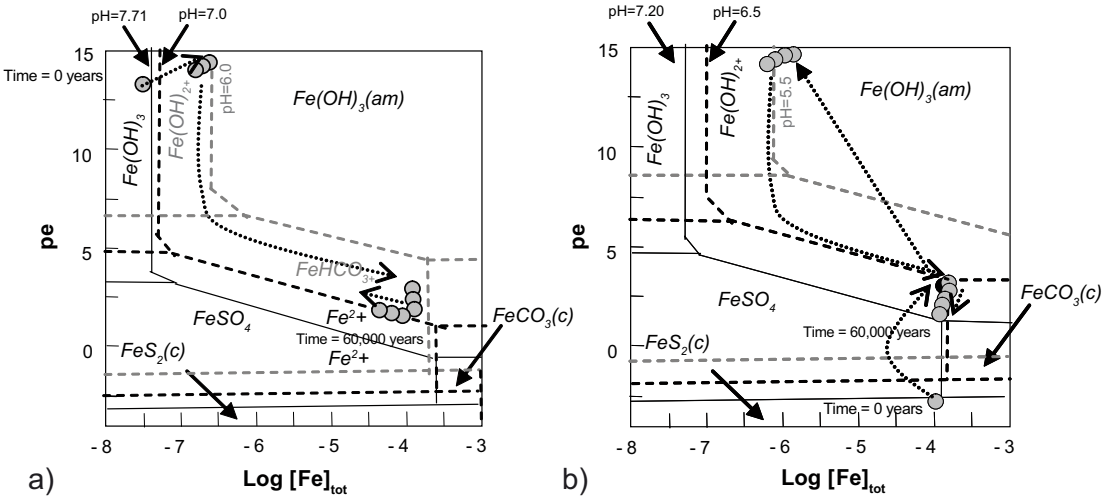

Figure 7-12. *Predominance area diagram at the tunnel-backfill boundary. T = 15°C. (pe = Eh(mV)/ 0.2T). a) Tunnel wall. pH = 6 to 7.7. $[C]_{tot}$ = 3.7·10^{-2}M (pH 6); 2.2·10^{-3}M (pH 7) and 4.6·10^{-4}M (pH 7.7). [S] = 5.2·10^{-3}M (pH 7.0 and 7.7); 2.2·10^{-2}M (pH 6). [Ca] = 2.3·10^{-3}M (pH 7.0 and 7.7); 3.0·10^{-2}M (pH 6). b) Backfill in contact with the tunnel wall (X = 17, Y = 0, Z = 20 m). pH = 5.5 to 7.2. $[C]_{tot}$ = 5.1·10^{-2}M (pH 5.5); 1.7·10^{-3}M (pH 6.5) and 2.3·10^{-3}M (pH 7.2). [S] = 3.8·10^{-2}M. [Ca] = 1.8·10^{-2}M. Grey circles are values given by the model at different times at the selected points.*

7.3 Iron hydroxide

The influence of the initial amount of $Fe(OH)_3$(am) in the oxidised zone formed in the tunnel wall during the first stage of the modelling have also been studied although its effect is not expected to be relevant because it is not a very good oxidant. Although the amount used as initial concentration in stage 2 is the result obtained in stage 1, we have performed a sensitivity analysis in order to check the influence of this mineral on the later backfill behaviour. In this case, we have considered that the initial concentration of $Fe(OH)_3$(am) precipitated on the tunnel wall is 3 orders of magnitude lower than in the base case, that is, 5.36·10^{-6} mole dm^{-3}. This variation does not produce any change in the initial pore water composition of tunnel wall area.

In both cases, groundwater entering in the backfill area has a high redox potential given that it has previously interacted with the oxidized layer around the tunnel. Because of that, pyrite in the backfill is dissolved and $Fe(OH)_3$(am) precipitates. The amount of $Fe(OH)_3$(am) precipitated in the backfill is directly related to the pyrite oxidised, that is, the maximum amount of iron oxihydroxide precipitated is obtained when pyrite finishes and it is 8.4·10^{-3} mole dm^{-3} water. In the case of considering siderite (Section 7.2) the maximum amount of $Fe(OH)_3$(am) precipitated in the backfill is obtained when both siderite and pyrite have completely dissolved and in this case it achieves values around 9.4·10^{-2} mole dm^{-3} water.

On the other hand, groundwater of the fracture in contact with the tunnel wall increases its redox potential by diffusion and due to the precipitation of $Fe(OH)_3$(am) in this area. The amount precipitated does not change when varying the initial concentration of $Fe(OH)_3$(am) in the tunnel wall because it mainly depends on the aqueous concentration of Fe in the groundwater, its pH and redox potential.

Thus, the results obtained from this sensitivity analysis suggest that a decrease of three orders of magnitude in the initial amount of $Fe(OH)_3$(am) in the tunnel wall does not produce any significant change in the final results. In fact, the control of the precipitation of $Fe(OH)_3$(am) is exerted by the dissolution of pyrite and/or siderite from the backfill. Only in case that $Fe(OH)_3$(am) of the tunnel wall was exhausted by dissolution, redox conditions will be controlled again by the groundwater. However, in all cases studied, and although dissolution is observed around 10,000 years, at the end of the modelling (60,000 years) the amount of $Fe(OH)_3$(am) has not significantly varied (Figure 7-13).

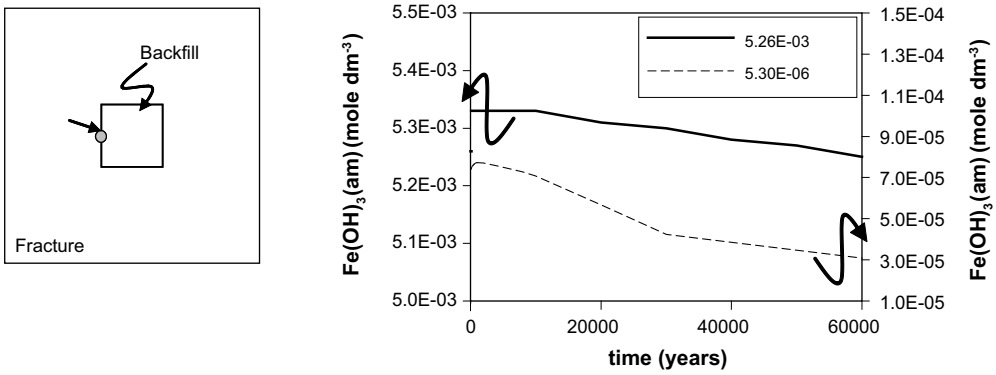

Figure 7-13. *Temporal evolution of the amount of $Fe(OH)_3(am)$ in the tunnel wall.*

7.4 Organic matter oxidation by microbial activity

Microbial respiration involves the oxidation of organic matter by different oxidants. In the present section, we are mainly interested in aerobic microbial respiration, where the electron acceptor responsible for the oxidation of organic matter is oxygen. Microbial activity is restricted under low water activities /see Masurat and Pedersen 2004 and references therein/, although its complete exclusion under the repository conditions cannot be ensured /see de La Cruz et al. 2005/. For this reason, we included this simulation in the present report, in order to assess which would be the potential influence of microbial activity on the evolution of the system.

As explained in detail in /Grandia et al. 2006/ the rate of dissolved O_2 consumption in the presence of microbes can be approached by a typical Monod expression (Equation 12) where $V_m \cdot S_{CH2O}$ stands for the maximum rate at a given biomass concentration and Kc_{O2} is the half saturation constant for oxygen.

$$R_{O_2}(moles \cdot dm^{-3}d^{-1}) = V_m \cdot S_{CH_2O} \frac{C_{O_2}}{Kc_{O_2} + C_{O_2}} \qquad \text{Equation 12}$$

Values reported in /Puigdomènech et al. 2001/ for these parameters are $V_m \cdot S_{CH2O}$ = 5 to 90 µM/day and Kc_{O2} = 200 to 300 µM. These values were obtained for a surface to volume ratio of 0.6 $m^2 \cdot dm^{-3}$ water in the REX experiment. If we consider that the more active microbes are those attached to surfaces, this would imply that the rate of oxygen consumption in $moles \cdot m^{-2} \cdot day^{-1}$ could be expressed as Equation 13, which, in order to be applied to a different system, needs to be corrected with the assumed coverage of surface area by microbes.

$$R_{O_2}(moles\,m^{-2}d^{-1}) = (5-90)10^{-6} \frac{moles}{dm^3 \cdot day} \frac{1\,dm^3}{0.6\,m^2} \frac{C_{O_2}}{(200-300)\cdot 10^{-6} + C_{O_2}} \qquad \text{Equation 13}$$

We assume that microbial aerobic respiration is not limited by the concentration of organic matter, and that the reaction for oxygen consumption can be simplified according to Equation 14.

$$CH_2O + O_2 = HCO_3^- + H^+ \qquad \text{Equation 14}$$

In this case, the surface area coated by microbes has been estimated equal to 10 $m^2 \cdot dm^{-3}$ by assuming that total surface area to volume ratio in the backfill is of the order of 100 $m^2 \cdot dm^{-3}$ and that only a 10% of the total surface is coated by microbes. This value will imply a concentration of microbes of 10^{-11} M (i.e. $6 \cdot 10^{12}$ cells/dm^3 water), which is close to the upper limit of the values found in subsurface environments, in the range 10^8–10^{11} cells/dm^3 /see Kotelnikova 2002/.

In this model initial and boundary conditions and pore water compositions are equal to the base case (Section 6.2.4). But we have considered two different cases: one assumes that pyrite is also present in the backfill in the concentrations reported in the base case and, the other assumes that there is no pyrite in the backfill, and thus, microbial consumption is the only sink of O_2. In both cases, organic matter is considered in excess.

When there is an initial amount of pyrite in the backfill, pyrite only dissolves during the first 20 years (Figure 7-14). At this time, it has completely dissolved in the contact with the tunnel wall but the dissolution front is smaller than in the base case (Section 6.2.5) or the siderite case (Section 7.2). This is because in the base case, only pyrite dissolution consumes O_2(aq) and to dissolve one mole of pyrite 3.75 moles of O_2(aq) are needed (Equation 15). In Figure 7-15 there is the saturation index of O_2(g) as a function of the distance at 30 years in order to see the difference of behaviour between the modelled cases (saturation indices instead of O_2(aq) concentrations are displayed as they are more sensitive to the differences). When considering siderite in the system, part of the oxygen is used to dissolve siderite and thus, the dissolution front of pyrite is slower because there is less O_2 available. Finally, when considering the

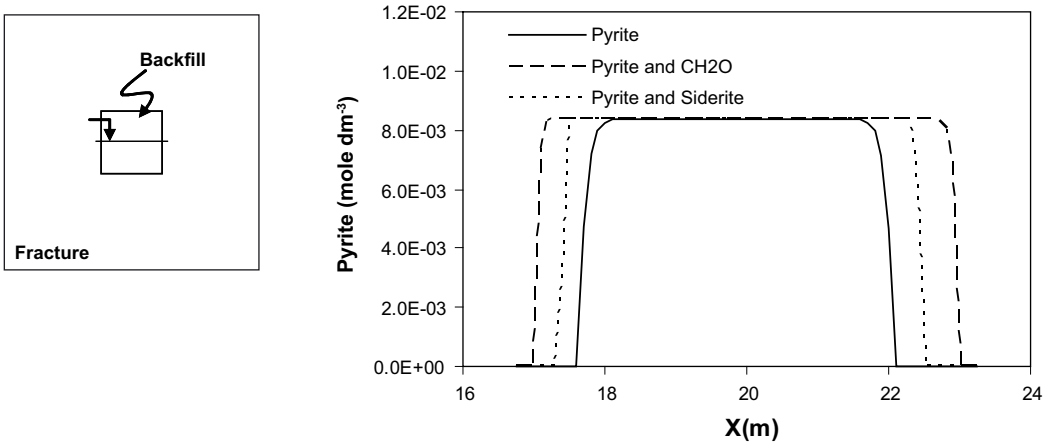

Figure 7-14. *Detail of the amount of pyrite remaining in the backfill system after 200 years for the base case (continuous line) and for the cases considering siderite (dashed line) and Organic matter (dotted line) (Z = 20 m).*

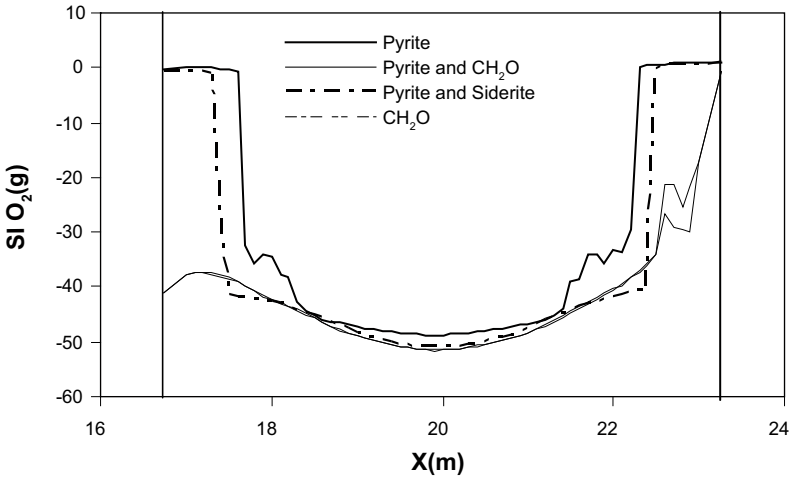

Figure 7-15. *Detail of saturation index of O_2(g) as a measure of the redox capacity of the system after 30 years for the base case (continuous line) and for the cases considering siderite (dashed-dotted line), organic matter (dashed line) and considering only organic matter (dotted line) (Z = 20 m).*

oxidation of organic matter, the amount of O_2(aq) available for pyrite oxidation is less than in the siderite case, because one mole of organic matter needs one mole of O_2(aq) to be oxidised (Equation 16) while one mole of siderite consumes only 0.25 moles of O_2(aq) (Equation 17).

FeS_2 (s) + 3.75 O_2 (aq) + 3.5 $H_2O \rightarrow Fe(OH)_3$ (am) + 2 SO_4^{2-} + 4H^+ Equation 15

$FeCO_3$ (s) + 0.25 O_2(aq) + 2.5 $H_2O \rightarrow Fe(OH)_3$ (am) + H^+ + HCO_3^- Equation 16

$CH_2O + O_2(aq) = HCO_3^- + H^+$ Equation 17

Again, the amount of iron hydroxide precipitated in the backfill is related to the amount of pyrite that dissolves. Then, when pyrite is not considered (only microbial consumption of O_2) there is no precipitation of $Fe(OH)_3$(am) in the backfill (Figure 7-16). And when pyrite is considered, the amount of $Fe(OH)_3$(am) precipitated equals the amount of pyrite dissolved and thus the higher the oxidation of pyrite, the higher the amount of precipitated iron(III) hydroxide. When both pyrite dissolution and microbial O_2(aq) consumption are considered, $Fe(OH)_3$(am) is observed in the backfill near the tunnel wall, where pyrite has been exhausted.

In the same way, the amount of gypsum precipitated in the system is lower when the oxidation of organic matter is considered. As pyrite is not dissolving as much as in the base case, there is less amount of sulphate in solution and gypsum does not precipitate as much as in the base case (Figure 7-17).

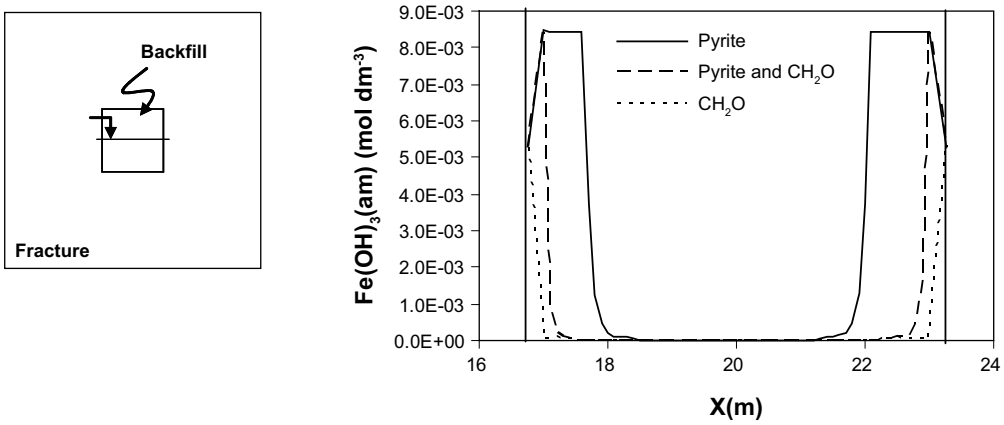

Figure 7-16. *Detail of the amount of $Fe(OH)_3$(am) precipitated in the backfill at 200 years for the base case (continuous line) and for the cases considering pyrite and organic matter (dotted line) and only organic matter (dashed line) (Z = 20 m).*

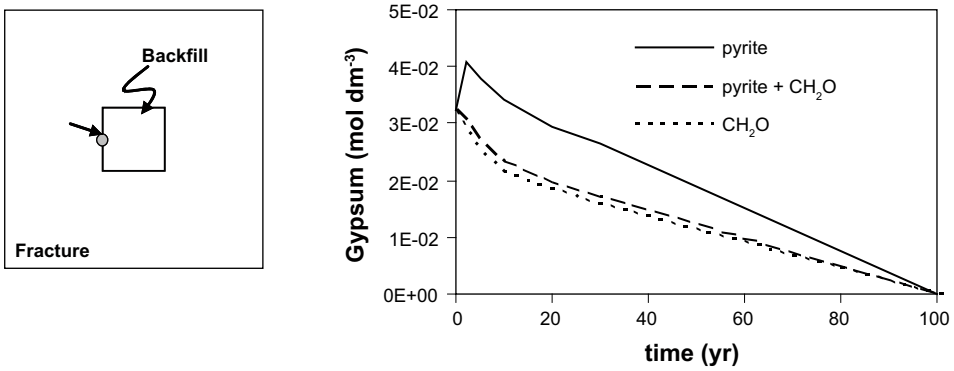

Figure 7-17. *Evolution of gypsum precipitated in the backfill (near the tunnel wall, X = 17.1 m, Z = 20 m) as function of time.*

The oxidation of CH_2O increases the total amount of HCO_3^- in the backfill pore water. This, together with the fact that the dissolution front of pyrite is slower, allows a major buffering of pH and also a major precipitation of calcite during the first years. After 100 years the plume of HCO_3^- has disappeared and the pore water composition is controlled by inflowing groundwater.

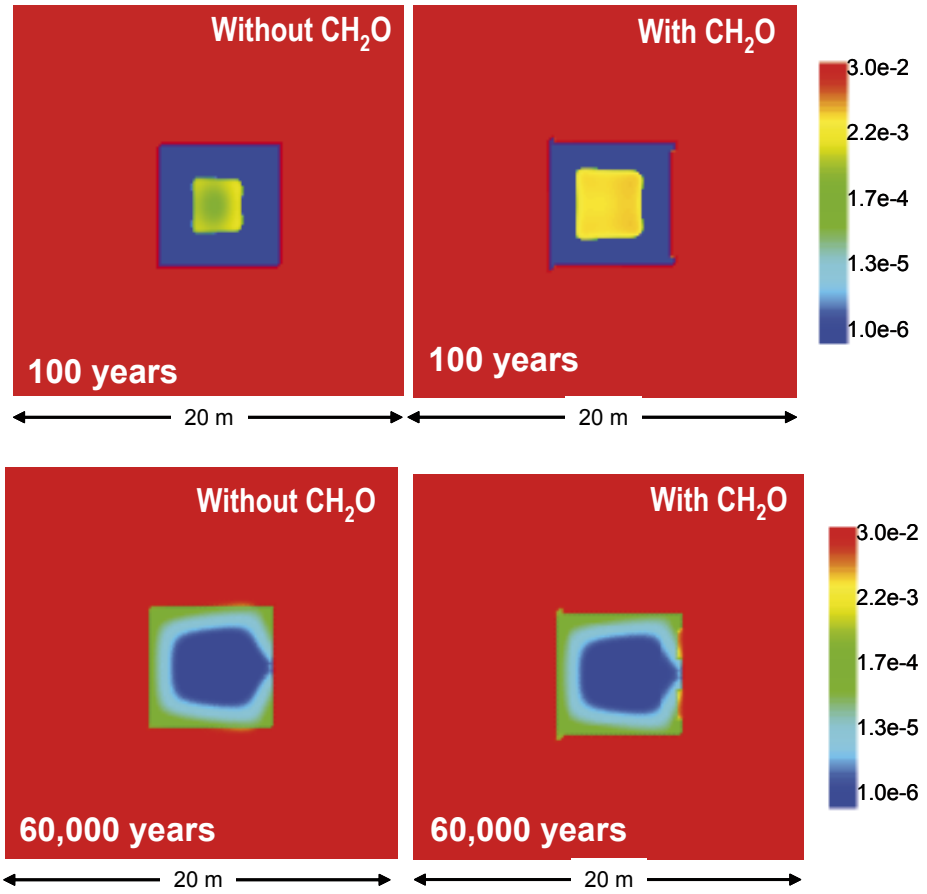

Figure 7-18. *Distribution of calcite in the system at 100 years (upper diagrams) and at 60,000 years (lower diagrams) for the base case (without CH_2O) and for any of the cases where consumption of CH_2O has been implemented. Values in mole dm^{-3} water.*

8 Summary and conclusions

The precipitation and dissolution of minerals in the area around the tunnel during the operational and the post-operational phase has been evaluated by building up a 2D model in which a fracture plane is perpendicularly intersected by the tunnel.

During the operational phase, whose duration has been assumed of 100 years, the tunnel is empty and the new water flow is assumed to be radial towards the tunnel walls. The area inside the tunnel has been assumed to be at a constant $O_2(g)$ and $CO_2(g)$ partial pressures, equal to the atmospheric values. Due to the high hydraulic gradients, the water flow towards the tunnel during the operational phase is rather fast (0.50 $dm^3\ min^{-1}\ m^{-1}$), therefore diffusion processes are not of relevance.

During the 100 years that the tunnel is assumed to be open, the results of the calculations indicate:

1) Calcite and iron(III) oxy-hydroxide precipitate during the operational stage of the repository on the tunnel wall due to the following processes:
   a) Degasification of $CO_2(g)$ of the initial groundwater containing $pCO_2(g) = 10^{-2.2}$ atm when in contact with the atmosphere inside the tunnel, with $pCO_2(g) = 10^{-2.2}$ atm, and subsequent calcite precipitation on the wall.
   b) Oxidation of pyrite at the tunnel wall due to the atmospheric $pO_2(g) = 0.21$ atm, and consequent formation of $Fe(OH)_3(am)$ on the wall.
2) The amount of calcite and $Fe(OH)_3(am)$ precipitated on the tunnel wall indicate average thickness of the layer of newly formed precipitates of 0.2 mm for calcite and 10 µm for $Fe(OH)_3(am)$ respectively, which are in agreement with determinations of coatings of these minerals in crystalline fractured media.
3) The amount of these minerals precipitated during the 100 years of the duration of the simulation does not imply any important variation on the porosity of the media, but will affect the future geochemical evolution of the groundwater entering the tunnel during the post-operational stage.
4) The increase of the iron concentration in the groundwater will cause a higher precipitation of $Fe(OH)_3(am)$ at the tunnel wall. This will not have any relevant influence on the groundwater composition as far as the amount of calcite present is able to buffer the pH decrease due to the process of $Fe(OH)_3(am)$. The assumption of an iron concentration in the groundwater exceeding the amount of calcite needed to buffer this pH decrease is not realistic due to the consequent supersaturation of the system with regards to iron solid phases that will prevent the aqueous iron concentration to reach these values.

The evolution of the system in the post-operational stage assumes that the tunnel is backfilled and water saturated (this is an approach followed due to numerical limitations, for detailed explanation see Chapter 6). The total time of the simulation has been extended to 60.000 years from the emplacement and saturation of the backfill. The main results of the calculations indicate that:

1) The redox control during the post-operational phase is exerted by the redox pair Fe(II)/$Fe(OH)_3(am)$. If siderite is present, the equilibrium $FeCO_3/Fe(OH)_3(am)$ exerts the redox control.
2) Any oxygen left in the rock during the operational phase will oxidise pyrite in the backfill during the first 200 years, with the consequent $Fe(OH)_3(am)$ precipitation. After this period, neither more dissolution of pyrite nor precipitation of Fe(III) phases is observed and the system is controlled by the incoming groundwater.

3) The inclusion of an initial amount of calcite in the backfill directly affects to the pH, buffering its value while pyrite is oxidised and decreasing the time that pH needs to achieve the values of the incoming groundwater.
4) The inclusion of an initial amount of siderite in the backfill reduces the dissolution front of pyrite and the length of the transitory state that the system needs to recover the pH values of the incoming groundwater.
5) In the post-operational phase, the inclusion of the oxidation of organic matter by microbial activity also reduces the dissolution front of pyrite and the length of the transitory state. Nevertheless, the hypothesis of the microbial activity in the backfill is doubtful, especially when the backfill used is compacted bentonite, given the lower water activity.
6) The composition of the exchange sites of the backfill evolves with time, producing an increase of calcium and magnesium in the cation exchange positions versus a decrease in sodium and potassium. The final cation exchange composition is controlled by the incoming groundwater.

Thus, the inclusion of carbonate minerals or organic matter oxidation causes a decrease of the time needed by pyrite to achieve a stationary state and to let the system to be controlled by the incoming groundwater composition (see Figure 8-1).

The consideration of a 3D model, where a section of the deposition tunnel would be considered away of the fracture zone, could be more realistic, as the transport in the third dimension can result in significant changes on the precipitation-dissolution of minerals and changes in the solute transport due to the modification in concentration gradients.

The precipitation of calcite and $Fe(OH)_3(am)$ in the tunnel wall during the operational phase can be seen as an additional sink for radionuclide retention giving that both minerals have high capacity of adsorption.

In the model presented here the precipitation of those minerals does not affect significantly the porosity of the fracture. However, it is important to note that in the rock matrix near the fracture, the porosity is lower and that the precipitation of minerals in the tunnel wall can have a more important consequence. Nevertheless, this is not an easy question to evaluate because other simultaneous processes such as grouting will affect the final geochemical background of the tunnel wall-backfill system.

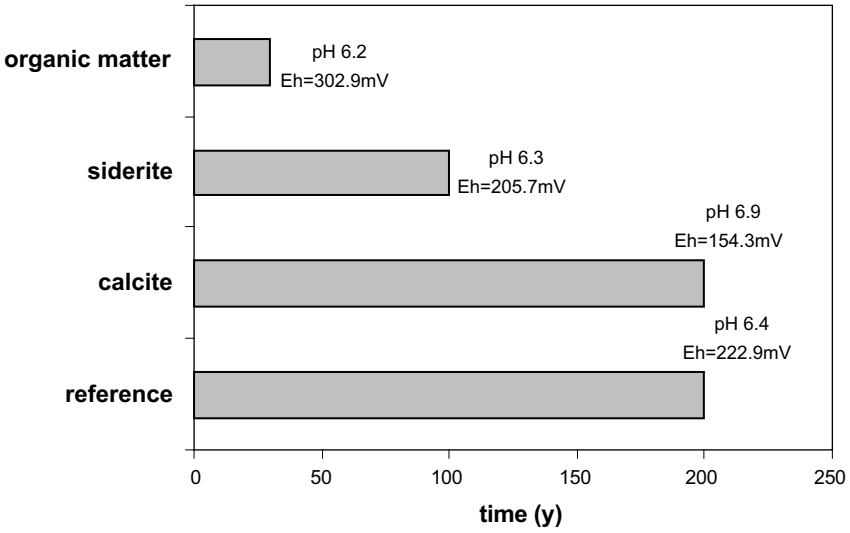

Figure 8-1. *Time needed for the pyrite of the backfill to achieve the stationary state for the reference case and for the cases where initial amounts of calcite and siderite and oxidation of organic matter are considered. Values of pH and of redox potential at this point are reported.*

9 References

Börgesson L, Fälth B, Hernelind J, 2004. Water saturation phase on the tunnel backfill in the KBS-3V concept and its influence on the wetting of the buffer. Preliminary report. Clay Technology.

Bradbury M H, Baeyens B, 2002. Porewater chemistry in compacted re-saturated MX-Bentonite. Physico-chemical characterisation and geochemical modelling. PSI Bericht, Nr.02-10. Waste Management Laboratory Report. Paul Scherrer Institut, Villigen, Switzerland.

de la Cruz B, Villar M V, Turrero M J, Peña J, Fernández A M, Carlsson T, Herbert H-J, Meyer T, Vokal A, Arcos D, 2005. Deliverable 1 of Component 2. STATE-OF-THE-ART REPORT. WP-2.1: Critical review and incorporation of information of EC, national and international programmes in RTD component 2. NF-PRO Project.

Dershowitz W, Winberg A, Hermansson J, Byegard J, Tullborg E-L, Andersson P, Mazurek M, 2003. Äspö Hard Rock Laboratory. Äspö Task Force on modelling of groundwater flow and transport of solutes. Task 6C. A semi-synthetic model of block scale conductive structures at the Äspö HRL. SKB International progress report; IPR-03-13.

Falck W E, Read D, Thomas J B, 1996. CHEMVAL2: Themodynamic Database – Final Report.- CEC Rep. EUR 16897EN: 164 p.

Grandia F, Arcos D, Domènech C, Duro L, 2006. Assessment of the oxygen consumption in the backfill. SKB-R-06-106. Svensk Kärnbränslehantering AB.

Guimerà J, Duro L, Jordana S, Bruno J, 1999. Effects of ice melting and redox front migration in fractured rocks of low permeability. SKB TR-99-19, 86 p. Svensk Kärnbränslehantering AB.

Guimerà J, Duro L, Delos A, 2006. Changes in groundwater composition as a consequence of deglaciation: implications for PA. SKB-R-report in print. Svensk Kärnbränslehantering AB.

Hartley L, Cox I, Holton D, Hunter F, Joyce S, Gylling B, Lindgren M, 2004. Groundwater flow and radionuclide transport modelling using CONNECTFLOW in support of the SR Can assessment. SKB R-04-61. Svensk Kärnbränslehantering AB.

Huertas F J, Caballero E, Jiménez de Cisneros C, Huertas F, Linares J, 2001. Kinetics of montmorillonite dissolution in granitic solutions. Applied Geochemistry 16, 397–407.

Hummel W, Berner U, Curti E, Pearson F J, Thoenen T, 2002. Nagra/PSI Chemical Thermodynamic Data Base 01/01. Universal Publishers. Florida, USA, 565 p.

Kipp K L, 1997. Guide to the revised heat and solute transport simulator, HST3D-version 2. U.S. Geological Survey Water Resources Investigations report 97-4157, 149 pp.

Kotelnikova S, 2002. Microbial production and oxidation of methane in deep subsurface. Earth Science Reviews 58, 367–395.

Luukkonen A, Pitkänen P, Partamies S, 2004. Significance and estimations of lifetime of natural fracture mineral buffers in the Olkiluoto edrock. Posiva WR 2004-08.

Madsen F T, 1998. Clay mineralogical investigations related to nuclear waste disposal. Clay minerals, 33, 109–129.

Masurat P, Pedersen K, 2004. Microbial sulphide production in compacted bentonite at the commencement of long-term disposal of high-level radioactive waste. In Scientific basis for nuclear waste management XXVII. Edited by Oversby V.M. and Werme L.O. Materials Research Society, Warrendale, Pennsylvania. pp 805–810.

Ochs M, Talerico C, 2004. Sr-Can. Data Uncertainty assessment. Migration parameters for the bentonite buffer in the KBS-3 concept. SKB TR-04-18, Svensk Kärnbränslehantering AB.

Parkhurst D L, Appelo C A J, 1999. User's guide to PHREEQC (version 2) – A computer program for speciation, batch-reaction, one-dimensional transport and inverse geochemical calculations. U.S. Geological Survey Water Resources investigations report 99-4259.

Parkhurst D L, Kipp K L, Engesgaard P, Charlton S R, 2004. PHAST. A program for simulating ground-water flow, solute transport and multicomponent geochemical reactions. USGS techniques and methods 6-A8, 154 pp.

Petersson J, Berglund J, Danielsson P, Wängnerud A, Tullborg E-L, Mattsson H, Thunehed H, Isaksson H, Lindroos H, 2004. Forsmark site investigation. Petrography, geochemistry, petrophysics and fracture mineralogy of boreholes KFM01A, KFM02A and KFM03A+B. SKB P-04-103, Svensk Kärnbränslehantering AB.

Puigdomènech I, Ambrosi J P, Eisenlohr L, Lartigue J E, Banwart S A, Bateman K, Milodowski A E, West J M, Griffault L, Gustafsson E, Hama K, Yoshida H, Kotelnikova S, Pedersen K, Michaud V, Trotignon L, Rivas Perez J, Tullborg E L, 2001. O_2 depletion in a granitic media. The REX project. SKB TR-01-05, Svensk Kärnbränslehantering AB.

Pusch R, 2001. The buffer and backfill handbook. Part 2: materials and techniques. SKB TR-02-12, Svensk Kärnbränslehantering AB.

Rickard D T, 1975. Kinetics and mechanism of pyrite formation at low temperatures. American Journal of Science, 275, 636–652.

SKB, 1999. Deep repository for spent nuclear fuel. Post closure safety. Main report. Volume I. SKB TR-99-06, Svensk Kärnbränslehantering AB.

SKB, 2003. Planning report for the Safety assessment SR-Can. SKB TR-03-08, Svensk Kärnbränslehantering AB.

SKB, 2004a. Interim main report of the safety assessment SR-Can. SKB TR-04-11, Svensk Kärnbränslehantering AB.

SKB, 2004b. Interim initial state report for the safety assessment SR-Can. SKB R-04-35, Svensk Kärnbränslehantering AB.

SKB, 2005. Buffer and backfill process report for the safety assessment SR-Can. Interim Report. Version 2005-06-14.

Wersin P, 2003. Geochemical modelling of bentonite pore water in high-level waster repository. Journal of Contaminant Hydrology, 61, 405–422.

Williamson M A, Rimstidt J D, 1994. The kinetics and electrochemical rate-determining step of aqueous pyrite oxidation. Geochimica et Cosmochimica Acta 58, 5443–5454.